

UNIVERSIDAD DE COLIMA



FACULTAD DE CIENCIAS

---

# **Simulations and analysis of Au+Au collisions at NICA energies for the MPD experiment**

---

THESIS BSC PHYSICS

*Author:*

Darío CHAIRES

*Supervisor:*

M. Elena TEJEDA-YEOMANS

May 15<sup>th</sup> 2020

# Contents

<b>1 Preface</b>	<b>2</b>
<b>2 Introduction</b>	<b>3</b>
2.1 Historical context . . . . .	3
2.2 Color confinement, asymptotic freedom and phase transitions . . . . .	4
2.3 The big picture of heavy-ion collisions . . . . .	7
2.4 Overview and main goals of MPD experiment at NICA . . . . .	9
<b>3 Simulation and analysis tools</b>	<b>12</b>
3.1 Analysis tools . . . . .	12
3.1.1 Center-of-Mass Energy . . . . .	12
3.1.2 Impact parameter . . . . .	14
3.1.3 Transverse momentum and angle of deflection . . . . .	15
3.1.4 Rapidity . . . . .	16
3.1.5 Pseudorapidity . . . . .	17
3.2 PHSD approach . . . . .	19
<b>4 Simulation results</b>	<b>22</b>
4.1 Results at generator level . . . . .	22
4.1.1 PHSD, 100 events, 11 GeV, Min.Bias . . . . .	23
4.1.2 PHSD, 100 000 events, 11 GeV, head-on collisions . . . . .	24
4.1.3 PHSD, 10 000 events, 11 GeV, Min.Bias . . . . .	26
4.1.4 UrQMD, 10 000 events, 11 GeV, Min.Bias . . . . .	31
4.2 Results using mpdroot framework . . . . .	34
4.2.1 BE-BE detector . . . . .	34
4.2.2 Inner detector MBB . . . . .	38
<b>5 Conclusions and future work</b>	<b>45</b>

## 1 Preface

The aim of this work is to study the processes that take place in heavy-ion collisions before we perform the actual experiment, from having control of the tools that help to classify the nature of the collisions at the beginning of the event, to getting familiarized with the tools used to analyse the final products of the events. To this end, I'll be using different software to simulate the collisions, gather the data and analyse it at different levels and I will compare with results reported in the literature or in other experiments.

The software I learned to use in order to simulate relativistic heavy-ion collisions is PHSD [1]. In order to simulate the detection of produced particles in an experiment, I learned to use the MPDROOT framework [2]. I used this to transport the generated products on PHSD, by the implementation of a series of geometries and functions that define and simulate the interactions between the particles and detectors.

Finally, I compare my results with results obtained in other analyses, specifically on the effect that implies the use of another generator called UrQMD [6] instead of PHSD. For this, I simulated two specific sets (one with each generator) with 10 000 events and the maximum collision energy intended to use at NICA. The analysis of the particles detected by two planned detectors (miniBeBe and BeBe), are the principal subjects of this work. The results of this work, have helped in the design and testing at simulation level of the proposed detectors (miniBeBe and BeBe) at NICA energies.

I have organised the presentation of the work I have done in the following manner: in Section 2 I give the historical context of the experimental developments of heavy-ion collisions up until today; in Section 3 I provide an overview if the main tools I have learned to use in order to characterize the initial and final state conditions in these type of collisions and I add a summarized version of the PHSD software I used to perform the simulations at NICA energies; in Section 4 I summarize the main results of the work I did both at the level of the collision simulation and at the level of the detector simulation; finally, I conclude and give a glimpse of future work in these directions in Section 5.

## 2 Introduction

### 2.1 Historical context

The 1974 workshop at Bear Mountain *BeV/nucleon collisions of heavy ions* was an imperative event for the heavy-ion physics, because after this celebration physicists began to think about heavy-ion collisions as a tool to understand the properties of matter under high energy and baryon densities. This workshop took place during a period when there was a firm development on the understanding of the structure of matter as a system of confined quarks, after the introduction of the asymptotic freedom property of QCD in 1973 by David Gross, David Politzer and Frank Wilczek. Even in this picture, a deconfinement phase transition was later proposed in the rough suggestion that matter was a "quark soup" at high densities.

At the time of the Bear Mountain Workshop, the development of heavy-ion experiments took considerable interest among physicists in Europe, U.S., and Japan. The very first ultra-relativistic heavy-ion collider was built at the Brookhaven National Laboratory (RHIC), the first idea was proposed back in 1983 during the open meeting of the Nuclear Science Advisory Committee and after a few years, as some ideas were discarded as well as projects abandoned, the RHIC entered in the conceptual stage. The funding began in 1990, starting the actual construction in 1991. The first run of the RHIC was on June 12, 2000, involving collisions of Au+Au at 28  $GeV$ .

On the other hand, in 1984 a Workshop with the CERN and the European Committee for Future Accelerators took place in Switzerland, in this event the concept of the construction of the Large Hadron Collider (LHC) obtained official recognition, the challenges of having high-energy collisions and what kind of particles to collide were discussed in this meeting as well. The addition of heavy-ion studies inside the LHC was proposed with the ATLAS detector in 1993 and was approved in 1997. The first experimental collisions of Pb+Pb at the LHC took place in November 2010, with an energy of 2.67  $TeV$ .

Between 1987 and 1992, the first superconductive synchrotron was built at the Joint Institute of Nuclear Research (JINR) as an upgrade of the Synchrophasotron (operational from 1957 to 2003), which worked with protons and deuterium nuclei. This modernization program made possible for the existing synchrotron to reach energy limits up to 7  $GeV$  by the implementation of superconductive magnets and also allowed the use of heavy-ions for the subsequent collisions. Since 2013, a new upgrade for the

Nuclotron has been in construction, the so-called Nuclotron-based Ion Collider fAcility (NICA), with the energy regime of  $\sqrt{s_{NN}} = 4-11$  GeV (see 3.1.1). This new regime will make possible to explore more deeply the phase diagram of QCD matter shown in figure 2.

## 2.2 Color confinement, asymptotic freedom and phase transitions

The theory of strong interactions in which nuclear interactions are included is best known to be explained using the Quantum Field Theory (QFT) framework, it takes the name of Quantum ChromoDynamics (QCD) where "chromo" stands for "color" analog to the electric charge in Quantum Electrodynamics (QED). QCD exhibits two particular aspects which can be addressed in heavy-ion collisions and hadron collisions in general: color confinement and asymptotic freedom.

If we imagine the not-so-simple scenario of a hadron conformed by two color-canceling (white color resulting) charged quarks interacting via strong force, "carried" by the mediator gluons, with a "weakly present" interaction (being awkwardly ironic) at distances of the order of  $10^{-15}$  m, this interaction will become "strongly present" if the distance between the quarks begins to increase. The amount of potential energy needed to perform this action is so big that instead of having two very separate quarks with their own color field, the energy is used to generate another two color-canceling quarks in the middle of the two originals. Conceptually, this scenario of colored quarks confined in a color-neutral hadron is what describes color confinement, yet unproven but well established in lattice QCD calculations and tested over decades of various experiments.

Now, this decrease in the interaction strength, formally called coupling, is given by an increase in the energy scale in which those interactions are present, this increase in energy corresponds to a decrease in the distance of the interactions. Moreover, these decreases in the coupling can be simplified with a linear relation to the distance, as some kind of color spring or rubber band. This characteristic behavior is what is called asymptotic freedom, and the strength of these interactions is given by the strong coupling constant  $\alpha_s = \frac{g_s^2}{4\pi}$ . The fact that this constant is not constant at all, but presents a "running" behavior is one of the principal aspects of QCD models at different energy regimes. This running is widely accepted in the theory of strong interactions as it has been tested experimentally as shown in fig 1.

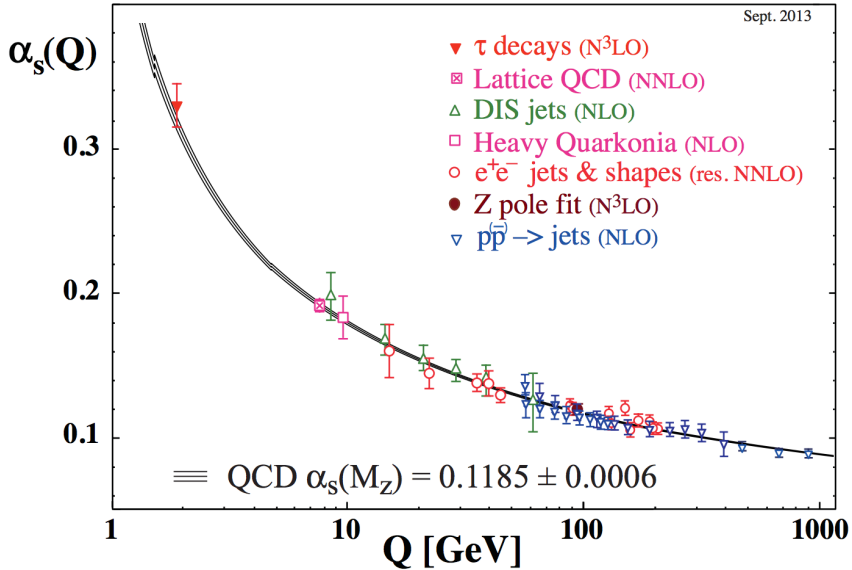


Figure 1: Different experiments and theoretical calculations show different values of  $\alpha_s$  in different energy regimes

As the protagonist particles in QCD are quarks and gluons, in which the former ones conform the baryonic matter (the well known "visible matter"), someone could expect the existence of different states of this kind of matter at a subatomic level, analogous to the phase transitions at a macroscopic level. As shown in Figure 2, it turns out that there is a QCD phase diagram, where these transitory states can be described in terms of the temperature and the chemical baryon potential. [3]

One of the most important reasons why heavy-ion collisions are studied is that these could tell something about the phase diagram of nuclear matter as a function of temperature and the net baryon density (excess of quarks over anti-quarks). The standard parameter to characterize the net baryon density is known as the baryon number chemical potential  $\mu_B$  (conjugate of baryon number density  $n_B$ ), where  $\mu_B = 0$  indicates an equal density of quarks over anti-quarks. This value of chemical potential is a good approximation for matter produced at RHIC and the LHC, as well as in the early universe. In all these cases, the confined hadronic matter forms by a crossover as the QGP expands. On the other hand theoretical studies predicts that at high baryon densities, QCD matter must undergo a first order phase transition. [4]. The phase diagram of baryonic matter is depicted in fig. 2

By decreasing the collision energies we increase  $\mu_B$ , and that region of the phase diagram can be scanned. Studies of heavy-ion collisions at lower energies are planned to be performed at the Nuclotron-Based Ion Collider Facility (NICA) in Dubna, and other facilities around the world. One of the main goals of the NICA project is to answer if there is a critical point (minimum energy collision) where the phase transition ends and turns into a smooth crossover.

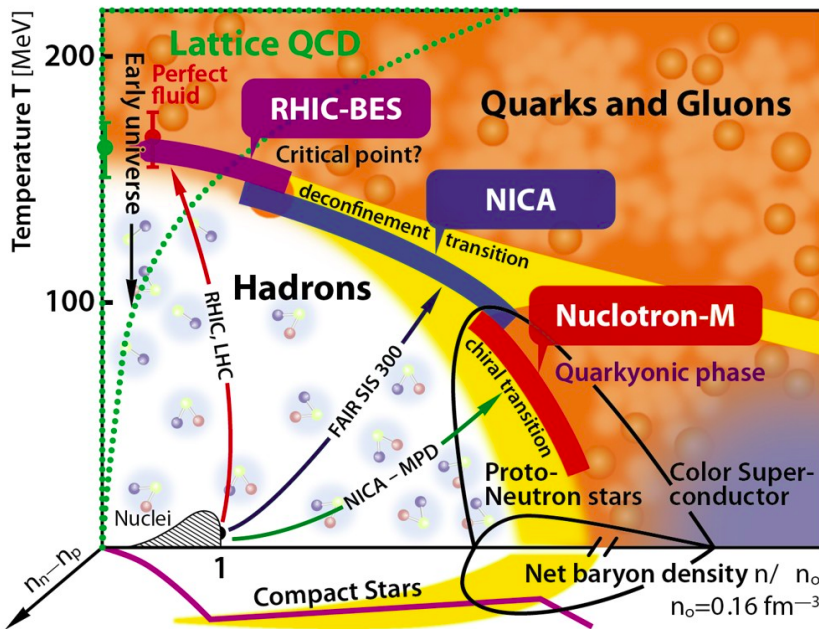


Figure 2: QCD matter phase diagram and the regimes covered by different projects are shown. NICA regime covers both collisions in which the confinement is no more and QGP is well formed, and collisions in which the matter is confined and remain its hadronic nature [4], [5]. Regimes of other projects are shown as well, being  $\sqrt{s_{NN}}$  of 7.7-39 GeV, 4-11 GeV and 0.44-4.5 GeV form the RHIC-BES, NICA and Nuclotron-M (first stage project of NICA) respectively.

On the other hand, lattice QCD results with  $\mu_B \sim 0$  (close to the temperature axis in the phase diagram) predict that the phase transition from hadronic to a deconfined phase is by a crossover, such that at a critical temperature both phases are indistinguishable, nevertheless such behaviour is predicted only for small net-baryon densities. For higher values of  $\mu_B$  models rely on effective theories of QCD. These models predict

two non-necessarily-coincident chiral and deconfinement transitions of first order which are coincident in the the regime of vanishing chemical potentials. Furthermore, these regions of first order phase transition and crossover should be separated by a critical point where the congruence of both transition line starts, a region of non-congruence between chiral and deconfinement transitions gives rise to a third state of matter called Quarkyonic matter. This QCD phase diagram has been explored in different experiments and studied with QCD based models taking different energy regimes, although there's a lot we don't know of it yet.

### 2.3 The big picture of heavy-ion collisions

As an introduction to heavy-ion collisions, it's good to get a qualitative description of the events after two ultrarelativistic nuclei collide in the center-of-mass frame. By Lorentz contraction, incident nuclei become disks of a diameter of a few femtometers, in fact, the thickness of the incident nuclei is contracted by a gamma factor  $\gamma$  which value is related to its velocity and rapidity and depends directly on the amount of energy used to accelerate the nuclei. Each disk has many color charged quarks and anti-quarks, these particles are sources of color fields and gluons, which carry color as well.

The area density of partons is not uniform across the disk, it increases with the velocity and has different fluctuations between nuclei. In general, we can see the incident nuclei as a system of partons (particles conforming nucleons) with a longitudinal momentum distribution very close to that of a superposition of individual nucleons, with modifications due to proximity and motion relative to other nucleons.

When two nuclei collide, most of the incident partons lose energy and are not deflected by any large angle and most of these interactions involve soft interactions, with a small amount of transverse momentum ( $p_t$ ). These interactions can be described in terms of interacting fields; as the two discs of strongly interacting transverse color fields and color charges collide, there is an exchange of color and longitudinal color fields that are produced, reducing the energy in the disks and then decay into quark-antiquark pairs and gluons. Other interactions between incident partons are hard perturbative interactions, these collisions although less probable have the particularity to reproduce similar results as the case of  $p + p$  collisions, there is a big exchange of momentum which lead to a production of particles with high  $p_t$ .

The maximum energy density in the two nuclei disks occurs as they collide, forming a system very far from equilibrium. It is more interesting to ask what happens to the

average energy density a specific time after the collision. After the collision, the high-energy-density is in constant expansion around the midpoint between the two disks, and at a relatively small time after the collision, the energy density still exceeds the energy density inside a typical hadron ( $500 \text{ MeV fm}^{-3}$ ). A big amount of entropy is produced in collisions as well since the final state after the collision is composed of many particles that lead to a system with large entropy, whereas before the collision the entropy is essentially zero.

With this in mind, we can hardly describe quarks and gluons produced in the collision as a collection of independent individuals. Quarks and gluons are strongly coupled, so they form a collective medium that expands as a relativistic hydrodynamic fluid, with a low ratio of viscosity to entropy density ( $\eta/s$ ). This medium is called quark-gluon plasma (QGP). The pressure-driven hydrodynamic expansion builds velocities of the order of half the speed of light, even if the transverse velocity of the fluid is small right after the collision. New QGP is continually forming as each disk starts to recede. This is because quarks and gluons produced at high rapidity are moving at speeds close to that of the light in the beam direction [8], and a long time passes in the lab reference frame in comparison with the QGP frame. In this process, each disk loses energy as partons with high rapidity separate from these, and QGP is produced. On the other hand, the particles with high- $p_T$  are produced at early times in the nuclei collision. The QGP formation ends at rapidities where most of the baryon number of the original nuclei end up. Once the production ends, individual volumes of QGP expand. Altogether, the droplet of QGP flows hydrodynamically as it cools. The expansion and cooling extend until the energy density of the fluid is less than that of an individual hadron, at this time the fluid falls apart into a mist of hadrons that scatter mutually and then recede away.

Another system to take to account is the remnants of the original nuclei, which have a high-baryon-density in it. This system expands and hydrodynamizes, forming a hot quark-rich QGP after a time of order  $1 \text{ fm/c}$  [8]. After the expansion and hydrodynamization, the QGP falls apart into hadrons, but given technological unavailabilities, the debris formed from these interactions has not been studied.

In reality, the volumes of QGP don't have a perfectly symmetric initial shape, due to the lumpiness in the energy density. These deviations from circular symmetry, given to non-central collisions or local changes in the energy density of the nuclei, resulting in anisotropies in the pressure of the hydrodynamic fluid [8], which affect the expansion

velocities and the azimuthal momentum distributions of the produced particles.

The rare hard collisions lead to the production of high-energy parton pairs at early times. The high-energy partons produce a jet of hadrons, photons, leptons, and/or heavy quark-antiquark pairs that traverse the region where the QGP is produced. This gives us information about the medium and the interactions in it.

## 2.4 Overview and main goals of MPD experiment at NICA

The NICA complex under development at JINR (Dubna), will be focused in the study of hot, dense and strong interacting baryonic matter by experiments involving colliding heavy-ions at ultra-relativistic velocities [5]. There are different theoretical models that suggest possible scenarios, the new experimental data coming from probes of heavy-ion collisions with high resolution and high statistics are imperative in order to test these theoretical predictions. The research program on heavy-ion collisions at the Nuclotron of the Joint Institute for Nuclear Research includes investigation of the reaction dynamics and nuclear equations of states, study of the in-medium properties of hadrons, production of (multi)-strange hyperons (baryons conformed by one or more heavy generation quarks) at the threshold and search for hyper-nuclei.

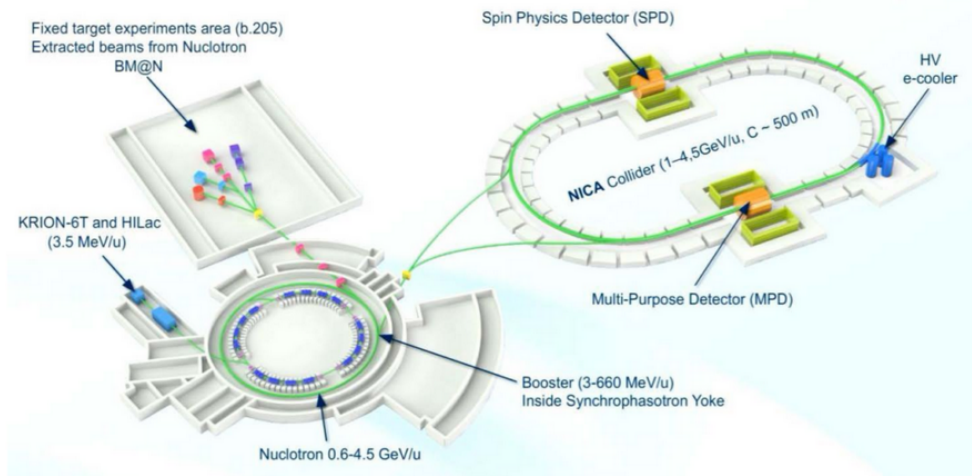


Figure 3: Basic structure of the NICA facility

The MPD facility [9] was proposed to explore the phase diagram of strong interacting matter in an environment of high multiplicity. One of the main goals of the experiments

on heavy ion beams is to discover and study a new form of QCD matter, the quark-gluon plasma [7]. Over the years, theoretical advances in QCD have lead to a significant complication of the phase diagram with the prediction of a critical point at intermediate temperatures and densities, one of the most important goals of the NICA project is the discovery of this critical point. Although the region of high baryon densities and low temperatures is considered hard to achieve in laboratory conditions, there are models that predicts this conditions naturally in neutron stars, it is expected the existence of a first order phase transition and the existence of a color superconductivity phase of matter.

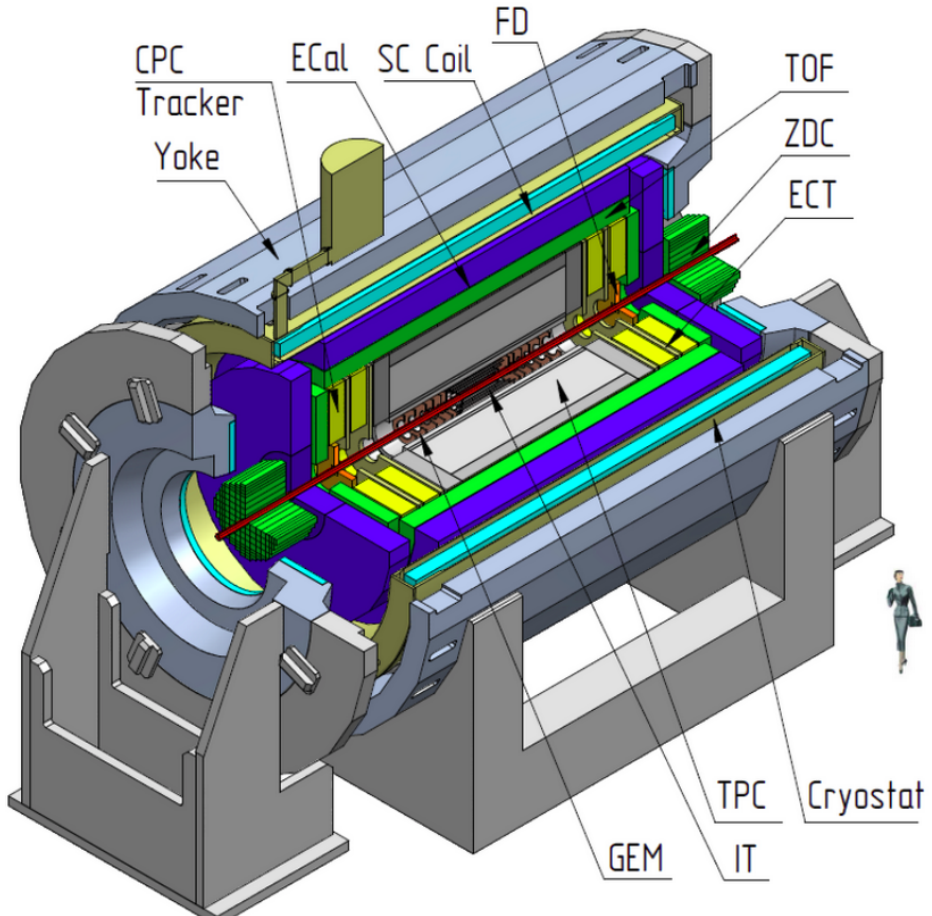


Figure 4: 3D layout of the MPD experiment

Some of the technical aspects of the MPD experiment is that as the average transverse momentum of the particles produced at NICA energies is relatively low, the material budget required for the detector designs is very low compared to experiments involving

higher energies.

For the purposes of this text, I will focus only on the inner detector (IT) and the central detector (CD) parts of the MPD, specifically on the beam-beam monitoring detector (BE-BE) and the mini BE-BE detector. To do it so, I'll work with Au+Au collisions using the PHSD event generator and test the effects of the produced particles in the detector named before.

During this text, I'll explain the principal tools needed to classify the initial conditions of the events and the tools needed to make the analyses. Then I'll report the analyses made at generator and detector levels. Finally I will conclude with the consequences of using this generator and give some ideas of the path for the future-work.

## 3 Simulation and analysis tools

On heavy-ion collisions experiments, there are several variables that describe and classify the nature of the events and make it easier to analyse the results. To classify the initial conditions of the simulated events, it is imperative to take into account that there are two options for colliding experiments; one where the momentum of the incident particles is equal and opposite and other where one of the particles is a fixed target. The advantage of the former choice is that we can assume that there is spatial symmetry and the center-of-mass is fixed at the moment of the events and therefore, ease the real measurements taken from the resulting data. On the other hand, the laboratory reference frame is where all the data is gathered, so the option of the inertial center-of-mass frame being fixed or moving with a constant velocity depends on the experiment settings I already mentioned above. Most of the observables and variables developed in this chapter will be analyzed from a fixed center-of-mass frame, unless explicitly expressed otherwise.

### 3.1 Analysis tools

Many of the variables needed for the analyses are taken directly from theoretical aspects or by establishing a convenient geometry over the environment where the measurements are made. In this subsection I will explain those quantities used to classify the simulations by its initial conditions, and the variables used to classify and analyse the products generated.

#### 3.1.1 Center-of-Mass Energy

In real experiments, the incident energy per beam is the initial condition for which control is completely taken at the collision events, therefore its importance in collider physics is imperative to perform further analyses. [10]

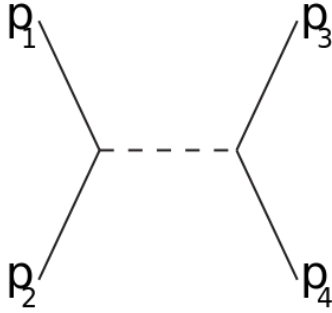


Figure 5: Two incoming particles with  $p_1$ , and  $p_2$ , they interact in some way and two particles with  $p_3$  and  $p_4$  are produced

Theoretically, the Mandelstam variables encode energy and the 4th-momentum in the same quantities. The one of interest in this view is the one that describes the square of the center-of-mass energy for two particles approaching with momentum  $p_1$  and  $p_2$  respectively(see figure 5):

$$s = (p_1 + p_2)^2 = p_1^2 + p_2^2 + 2p_1 \cdot p_2 \quad (1)$$

But the 4-momentum has components  $(E_1, -\vec{p}_1)$  and  $(E_2, -\vec{p}_2)$  (using the metric convention  $[+, -, -, -]$ ), therefore

$$s = E_1^2 + E_2^2 - \vec{p}_1^2 - \vec{p}_2^2 + 2E_1E_2 - 2\vec{p}_1 \cdot \vec{p}_2$$

Taking  $E_i^2 = m_i^2 + \vec{p}_i^2$

$$s = m_1^2 + m_2^2 + 2E_1E_2 - 2\vec{p}_1 \cdot \vec{p}_2 \quad (2)$$

In actual beam-beam colliders, the setting for the three-momentum is  $\vec{p}_1 = -\vec{p}_2$  and  $m_1 = m_2$  for the masses, therefore equation (2) can be written as

$$s = 4m^2 + 2\vec{p}^2 \quad (3)$$

In a frame where  $m_2$  is at rest ( $\vec{p}_2 = 0$ ), then the total momentum of the system can be expressed in terms of  $\vec{p}_{1lab} = 2\vec{p}_1$ , with this in mind we can express equation (2) as

$$s = 2m^2 + 2E_1m \quad (4)$$

The equation (4) express the energy per particle pairs in a fixed target experiment, therefore every particle involved has an incident center-of-mass energy given by  $\frac{\sqrt{s}}{2}$ , then the total center-of-mass energy for he incident nuclei is given by  $E_{cm} = A\sqrt{s}$ , where  $A$  is the atomic mass.

For the case of heavy-ions collisions, the quantity that defines the center-of-mass energy is taken per nucleon-nucleon pair, nevertheless, given that most nuclei are conformed by an unequal number of protons and neutrons, the proportion of energy needed to accelerate just one proton will differ significantly the greater the difference between nucleons. The expression that establish the fraction of the energy needed to make two protons collide with certain value of  $s$  is directly reflected on the momentum of the protons,  $p_{proton}$ , at the moment of the collisions

$$p_N = \frac{Z}{A} \cdot p_{proton}$$

Here  $Z$  stands for the number of protons conforming the nucleus and  $A$  is the atomic mass.

When  $p_N$  is used to express the center-of-mass energy in terms of  $s$ , we expressed in a more fashioned way:  $\sqrt{s_{NN}}$  [11].

### 3.1.2 Impact parameter

The main difference between p+p and A+A collisions is that just a very few nucleon collisions will be head-on. These hard collisions reproduce similar conditions and products for p+p events. As it is presented in fig. 6, the presence of soft interactions in the overlap region and a significant amount of nucleons that will just follow the beam direction without any collision involved, are the principal reason why heavy-ion collisions are studied separately.

The impact parameter is defined as the perpendicular distance between the the nuclei beams, normally denoted as  $b$ .

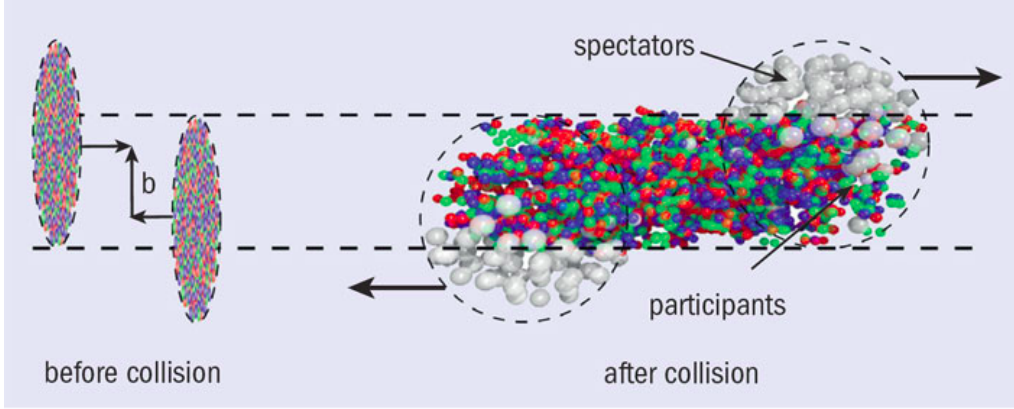


Figure 6: Graphic representation of two nuclei discs approaching with a distance  $b$  from their center

Collisions can be classified by its impact parameter, which value has a direct impact in the classification of the centrality of the collisions. Although the impact parameter can not be measured explicitly in real-life experiments, the multiplicity (number of particles created after the collision) in each event grows as the configuration of collisions present a more central setup. This is because the color force acts in a very short range, it becomes harder to confine quarks that are more than a nucleon's radius distance of each other. Therefore, part of the strong interactions are suppressed in the peripheral area. Therefore, at more central collisions, the partons involved in the overlap region have a higher probability to interact in some way, this makes the particle multiplicities a good inference of the centrality involved in the collisions. In fact, the multiplicity of charged particles is what commonly is used to measure centralities, as these are much easier to detect in real life than neutral particles.

### 3.1.3 Transverse momentum and angle of deflection

As particles are generated after the collision, they are deflected by an angle  $\theta$  and a momentum  $\vec{p}$  with three spatial components ( $p_x, p_y, p_z$ ), both quantities can be inferred by the use of detectors. Nevertheless, the projection of  $\vec{p}$  in the x-y axis, called transverse momentum or  $p_t$ , has also an angle  $\varphi$  related to it. Normally in collider physics, the momentum is associated with these two quantities and the *pseudorapidity*, which is related to the angle  $\theta$  (see section 3.1.5), so that  $\vec{p} = (p_t, \eta, \varphi)$ .

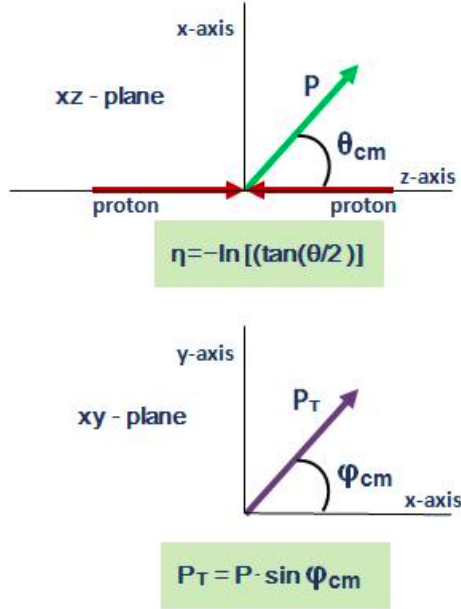


Figure 7: Diagram of  $\vec{p}$  from the center of mass frame and  $p_t$  form the transverse plane

As  $p_t$  is just a projection of the magnitude of  $\vec{p}$  in the transverse plane, it is straightforwardly obtained with basic trigonometry:

$$p_t = \sqrt{p_x^2 + p_y^2}$$

As for the angle that goes from the z-axis to the x-y plane:

$$\theta = \arctan\left(\frac{p_t}{p_z}\right)$$

since  $p_z = |p| \cos \theta$  and  $p_t = |p| \sin \theta$

### 3.1.4 Rapidity

Given the matrix form of Lorentz transformations in one direction:

$$\Lambda(y) = \begin{pmatrix} \cosh y & -\sinh y \\ -\sinh y & \cosh y \end{pmatrix}$$

We define the rapidity  $y$  as the hyperbolic angle between two referential frames. From this we can see that

$$\cosh y = \gamma = \frac{1}{\sqrt{1 - (\frac{v}{c})^2}}$$

$$\sinh y = \beta \gamma = \frac{v/c}{\sqrt{1 - (\frac{v}{c})^2}}$$

However in experimental particle physics rapidity is defined in a convenient way: If we take the rest energy and the momentum parallel to the beam axis as

$$E = \gamma mc^2 = mc^2 \cosh y$$

$$p_z = \gamma mv_z = mc \sinh y$$

Then we obtain

$$y = \operatorname{arctanh} \frac{p_z c}{E}$$

which in logarithmic form is

$$y = \frac{1}{2} \ln \left( \frac{E + p_z c}{E - p_z c} \right) \quad (5)$$

Now we can see how rapidity changes performing a Lorentz boost in the components of the 4-momentum:

$$\begin{aligned} y' &= \frac{1}{2} \ln \left( \frac{\gamma E/c - \beta \gamma p_z + \gamma p_z - \beta \gamma E/c}{\gamma E/c - \beta \gamma p_z - \gamma p_z + \beta \gamma E/c} \right) \\ &= \frac{1}{2} \ln \left( \frac{\gamma(E/c + p_z) - \beta \gamma(E/c + p_z)}{\gamma(E/c - p_z) + \beta \gamma(E/c - p_z)} \right) \\ &= \frac{1}{2} \ln \left( \frac{E/c + p_z}{E/c - p_z} \frac{\gamma - \beta \gamma}{\gamma + \beta \gamma} \right) \\ &= y + \ln \sqrt{\frac{1 - \beta}{1 + \beta}} \end{aligned}$$

which can be reduced to

$$y' = y - \operatorname{arctanh} \beta$$

This final expression has an important consequence when taking two values of rapidity  $y_1$  and  $y_2$ , when this quantities are measured by other inertial observer the difference of the rapidities is boost invariant along the z-axis:

$$y'_1 - y'_2 = y_1 - y_2 \quad (6)$$

### 3.1.5 Pseudorapidity

The problem with rapidity is that it can be hard to measure at ultra-relativistic limits, since at these velocities usually is difficult to get the total momentum of a particle especially when its z component is large. Here is when the concept of pseudorapidity  $\eta$  comes in handy for highly energetic particles:

We start by expressing  $E$  in terms of the momentum and rest mass and plug it in equation (3)

$$\begin{aligned}
y &= \frac{1}{2} \ln \left( \frac{\sqrt{p^2 c^2 + m^2 c^4} + p_z c}{\sqrt{p^2 c^2 + m^2 c^4} - p_z c} \right) \\
&= \frac{1}{2} \ln \left( \frac{pc \sqrt{\left(1 + \frac{m^2 c^4}{p^2 c^2}\right)} + p_z c}{pc \sqrt{\left(1 + \frac{m^2 c^4}{p^2 c^2}\right)} - p_z c} \right) \\
&\simeq \frac{1}{2} \ln \left( \frac{pc + p_z c + \frac{m^2 c^4}{2pc} + \dots}{pc - p_z c + \frac{m^2 c^4}{2pc} + \dots} \right) \\
&\simeq \frac{1}{2} \ln \left( \frac{1 + \frac{p_z}{p} + \frac{m^2 c^4}{2p^2 c^2} + \dots}{1 - \frac{p_z}{p} + \frac{m^2 c^4}{2p^2 c^2} + \dots} \right)
\end{aligned}$$

In the second expression I factored  $pc$  out of the square root and make a binomial expansion for a highly relativistic particle with  $pc \gg mc^2$

By symmetry  $\frac{p_z}{p} = \cos \theta$ , where  $\theta$  is the angle between the particle trajectory and the beam, therefore using the double angle cosine identity

$$1 + \cos \theta = 2 \cos^2 \frac{\theta}{2}$$

and

$$1 - \cos \theta = 2 \sin^2 \frac{\theta}{2}$$

And given that the third therm in the logarithm is negligible, we obtain

$$y \simeq \frac{1}{2} \ln \frac{\cos^2 \frac{\theta}{2}}{\sin^2 \frac{\theta}{2}}$$

or

$$y \simeq -\ln \tan \frac{\theta}{2}$$

The pseudorapidity is commonly used for highly relativistic particles because in real experiments, the momentum vector of a particle is hard to measure. What is important about this quantity is that for  $pc \gg mc^2$ , rapidity and pseudorapidity are approximately equal.  $\eta$  is defined as

$$\eta \equiv -\ln \tan \frac{\theta}{2} \tag{7}$$

The relation of  $\theta$  and  $\eta$  can be determined by the geometry of the events as:

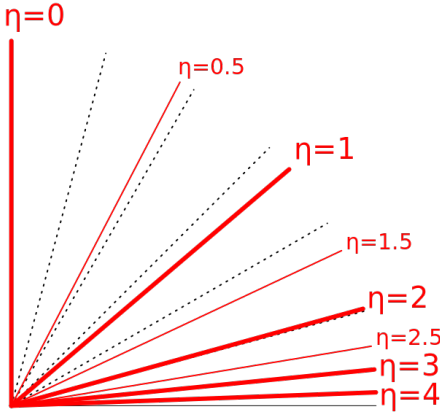


Figure 8: Geometric representation of  $\eta$

The analogy of the pseudorapidity and the angle from the beam axis at which the particles travel can be seen in the previous graph, where  $\eta = 0$  represents  $\theta = 90^\circ$  and  $\eta$  rapidly goes to infinity as  $\theta$  approaches  $0^\circ$

### 3.2 PHSD approach

The **Parton-Hadron-String Dynamics** transport is a dynamical approach generator for strongly interacting systems in and out-of equilibrium. It simulates the dynamics and transition of both parton and hadron phases, incorporating its degrees-of-freedom. The QGP stage is included in terms of quasiparticles with further hadronization and final interactions in the late stage. In this way, PHSD covers the full time evolution of relativistic heavy-ion collisions.

The impact parameter ranges  $[b_{min}, b_{max}]$ , the center-of-mass energy, the final propagation time  $t_{max}$ , and the type of ions to collide, can be selected to specify the initial conditions of the events.

To define which nuclei we are colliding, we have to express explicitly the mass of the incident particles and the number of protons with which they are formed. As PHSD is programmed to collide particles in a fixed-target configuration, we have to express the target mass, protons in the target, the projectile mass and protons in the projectile, with the quantities MASSTA, MSTAPR, MASSPR, MSPRPR respectively.

The impact parameter can be chosen in three different ways. The first is by the

*Min.Bias* probability distribution given by:

$$P(b) = \frac{2\pi b}{\int_{b_{min}}^{b_{max}} 2\pi b db} \quad (8)$$

with this case, the impact parameter is randomly chosen following this linear distribution. What this distribution tell us is that the probability of choosing a certain value of  $b$  increases linearly for greater values of  $b$ . [1]

The second way is to take a fixed value of  $b$  in every event, which is obtained taking the expected value

$$\langle b \rangle_{Min.Bias} = \int_{b_{min}}^{b_{max}} b P(b) db$$

The third way is to calculate the impact parameter over the range  $[b_{min}, b_{max}]$  with fixed steps given by a constant probability.

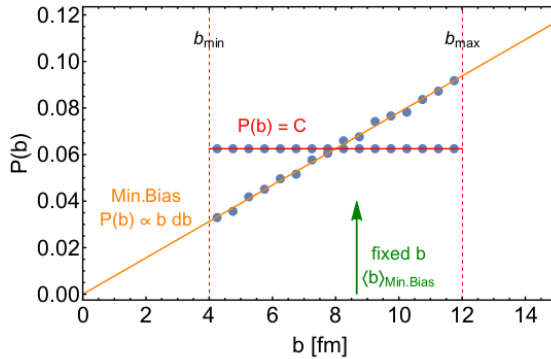


FIG. 2.1: Probability distribution  $P(b)$  as a function of the impact parameter  $b$  in PHSD. One can use a fixed impact parameter, or a range  $(b_{min}, b_{max})$ , or the minimum bias distribution (see text for explanations).

Figure 9: Mi.Bias distribution as a function of the impact parameter  $b$ . The fixed impact parameter mode, the step mode and the minimum bias option are shown in the range  $b \in [4, 12 \text{ fm}]$ . Figure extracted from PHSD manual [1].

The second parameter for the initial conditions is **ELAB**, which represents the bombarding kinetic energy per nucleon in the laboratory frame. It is related to the center-of-mass energy  $s_{NN}$  by

$$s_{NN} = 2 \times m_N \times (ELAB + 2m_N) \quad (9)$$

where  $m_N = 0.938 \text{ GeV}$

The PHSD approach has the fixed target setting as a default, from this setting, equation (8) can be obtained if we remember that the energy beam of one nucleon is

given by  $\sqrt{s_{NN}}/2$  and change some conventions of the system from which equation (4) was obtained. Firstly, as it is a fixed target system for particles of the same species, we will take  $m_{NN} = m_1 = m_2$ ,  $\vec{p}_{lab} = \vec{p}/2$  and  $E_1 = ELAB$ . This configuration was chosen since the actual quantity that is computed is taken from the center-of-mass energy in a beam-beam setting. This change of frame in the equation (4) leads to:

$$\frac{s_{NN}}{2} = 2m_N^2 + ELAB \ m_N$$

where  $ELAB$  takes just one half of the incoming energy in the beam-beam setting. Multiplying this quantity by two, leads to equation (8) where we are taking the energy of both beams.

The next table shows the relation between  $\sqrt{s_{NN}}$  and  $ELAB$  for some of the energies in the range planned to run at NICA.

ELAB (GeV)	$\sqrt{s_{NN}}$ (GeV)
6.65	4
11.45	5
17.31	6
24.24	7
32.23	8
41.30	9
51.42	10
62.62	11

For the next chapters, all the analyses were performed for events with  $\sqrt{s_{NN}} = 11$  GeV, which corresponds to  $ELAB = 62.62$  GeV, although for simplicity the center-of-mass energy nomenclature will be explicitly shown.

## 4 Simulation results

For this section, the results obtained are divided in the ones coming from the PHSD and UrQMD (Ultra relativistic Quantum Molecular Dynamics) generators and those that came when the particles generated are transported to the miniBeBe and BE-BE detectors. Great part of the work made here was to develop a few macros for the PHSD generator and adapt some others previously developed by Luis Valenzuela and Pedro Nieto, current members of the MexNICA collaboration, for the UrQMD generator in order to make them capable to read the PHSD output file structure. All the programs used for these analyses can be looked-up in the repository link showed on the bibliography. [12]

### 4.1 Results at generator level

In this section I will analyze different outcomes from events generated with the PHSD approach using different initial parameters. The histograms for the pseudorapidity and angle of deflection distributions were made using ROOT and the data generated from the PHSD output files.

The purpose of the histograms is to summarize graphically the distribution of an univariate data set, this allows to analyze the presence of outlier values, the skewness and in general get a simpler view of the statistics. In this way, these features give strong indications of a proper distributional model for the data. The most common form of histograms is obtained by splitting the range of data values (commonly fixed to the horizontal axis) in equal sized bins, then for each bin the number of data points are counted, giving us a certain amount of "entries" (fixed to the vertical axis) just for that bin. In other words, as the data set spans all of its values in the horizontal axis, every bin than splits this axis gets an amount of counts represented in the vertical axis.

As the simulations on PHSD model collisions or events that present an specific amount of generated particles which values depend on parameters such as number of nucleons and the impact parameter which actually follows a probability distribution (see 9), an increment of generated particles is expected if the number of events is increased and vice versa. On the other hand, the mean value of the entries should be in some way independent from the number of events the are analyzed, here is where a normalized variant of the histogram comes in handy. To achieve these variation, every bin is divided by the total number of entries, this is, the entries are normalized to sum one, this is the

intuitive case where the height of the histogram bar represents the proportion of the data in each bin.

The following histograms were obtained from different data sets, where the number of events vary. The normalized variant was used in order to obtain similar values for the mean entries per bin, with this it will be easier to see if, let's say, the Min.Bias distribution is on point, of course the statistical error will be reduced as the number of events is increased.

#### 4.1.1 PHSD, 100 events, 11 GeV, Min.Bias

The first simulation was made with 100 events for Au+Au collisions at 11 GeV, although is a very small sample it was useful to test the capabilities of the PHSD code and use different settings if the results are unwanted. For the sake of this document, this simulation was made just to test if the Min.Bias probability was implemented correctly during the selection of the impact parameter.

The first thing that can ensure that the Min.Bias probability was used to choose the impact parameter in each event is to draw their distribution, to check this distribution in the first place is strongly advised since the results may change consistently if other settings for the impact parameter were taken.

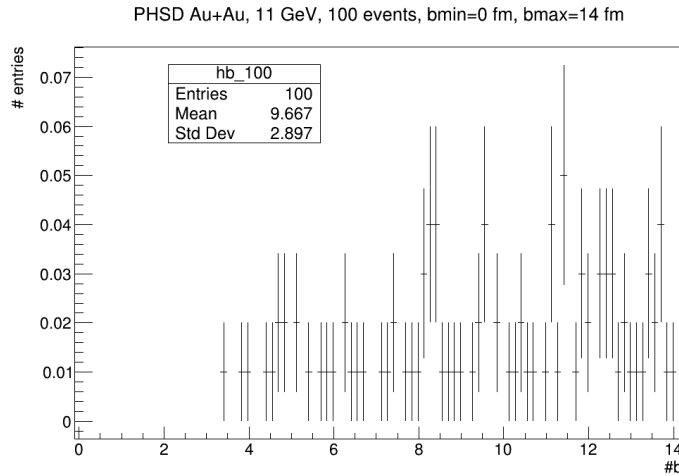


Figure 10: Distribution of the impact parameter for 100 randomly chosen values

With the distribution obtained is difficult to make a resemblance to the Min.Bias probability distribution of the PHSD code, it is hardly to infer that there's a linear

relation (see Fig. 9). It is expected that the more events show this behavior, the more accurate the probability distribution can be reproduced.

#### 4.1.2 PHSD, 100 000 events, 11 GeV, head-on collisions

A second simulation with a bigger sample of two gold nuclei at  $\sqrt{s_{NN}} = 11$  GeV, with  $b=0$  for all the 100 000 events. The pseudorapidity distribution of the final particles was drawn with the main purpose of observing the repercussions of head-on ideal collisions at the multiplicity level. Although this simulation results give a lot more of junk data and head-on events are less probable in real experiments, for means of the importance of  $b$  in the byproducts created after the collisions, it is interesting to approach this configuration.

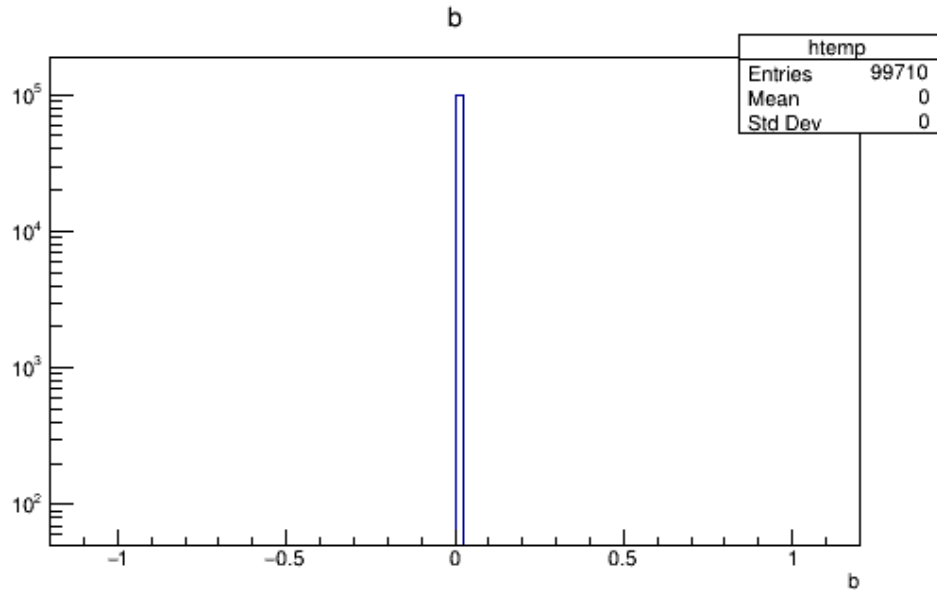


Figure 11: Fixed impact parameter distribution, all events lie in the same bin with  $b = 0$

The very first thing to note, again, is the impact parameter distribution with a fixed value equal to 0 for all the events, in this diagram we can see the behavior of the Min.Bias distribution when one takes the mean value at  $b = 0$ .

On the pseudorapidity distribution, the peaks at  $\eta = 4$  and  $\eta = -4$  are not present since we expect that most of the particles generate with high  $p_t$  values, and that's the reason why there's a highly steeper peak at  $\eta = 0$  in comparison to the simulation with Min.Bias, as it seen in fig. 12 distribution.

Another important note here is that given the high multiplicity, specifically in the mid rapidity region, some of the particles became virtually indistinguishable, making it hard to suggest a specific physical phenomenon to make bias for the byproducts.

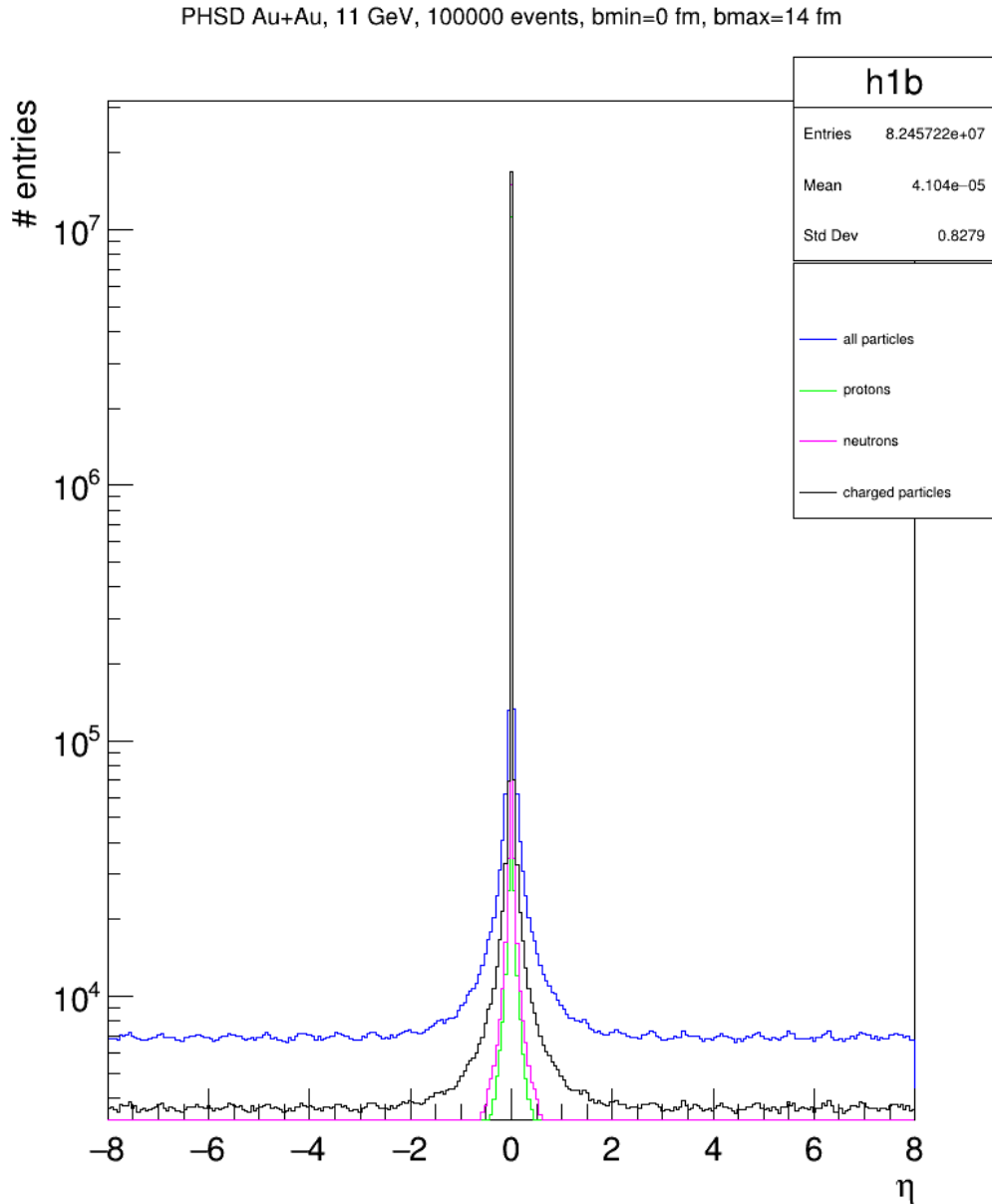


Figure 12: Pseudorapidity distributions for different set of particles, the high multiplicity at the center makes them graphically impossible to distinguish

As with respect to the PHSD output, the code allows us to identify the history of the particles measured in the distributions. This is, PHSD tells us how or from which particles they come from.

For this case I selected pions coming from the parton phase, specifically coming from non-string formations from quark-antiquark pairs, pions formed by quark-antiquark string pairs and pions coming from recombination.

The non-string pion formations come from the overlap region where the nucleons collide head-on and the distances between partons is so short that they can interact strongly to form another arrangement of quarks besides the known nucleons. These pions should be present in the high transverse momentum region.

On the other hand, the string formation of pions should come from the overlap region where the nucleons don't collide head-on, but they are sufficiently close to interact in some kind of way and get quark-antiquark pairs confined by the closeness of colored string fields. These pions should be the ones we can see between the middle and the ends in the angle distribution, and the straight tails we see in the pseudorapidity distribution. An important note here is that these three reactions conform most of the pions that we see in the distributions without making bias of their history.

#### 4.1.3 PHSD, 10 000 events, 11 GeV, Min.Bias

A simulation of two gold nuclei at  $\sqrt{s_{NN}} = 11$  GeV, with  $b \in [0, 14]$  randomly chosen by Monte-Carlo procedure was run and different histograms were made using the framework ROOT.

For the impact parameter setting, a total of 1000 values of the impact parameter were selected, each of them with 10 parallel events giving a total of 10 000 simulated collisions.

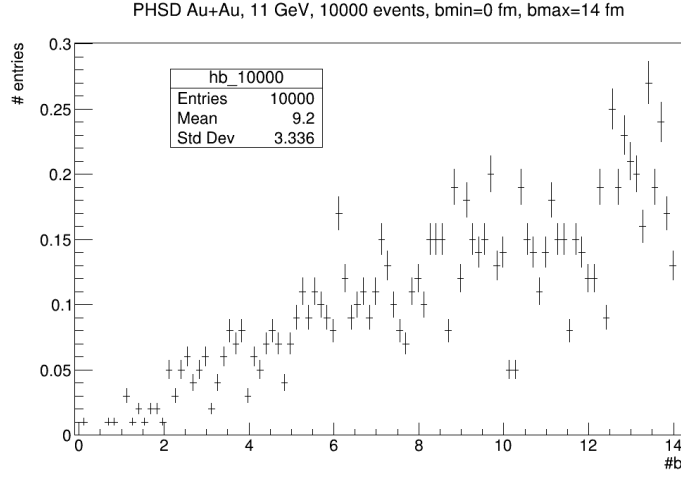


Figure 13: Distribution of the impact parameter for 1000 randomly chosen values

In this case is relatively easy to see that it follows the Min.Bias distribution since as the impact parameter increases so does the number of events involved with it, this reinforces that the probability of choosing a certain value of  $b$  increases linearly as the impact parameter takes greater values (see figure 9).

The  $\theta$  distribution gives us a rough idea of the direction of every particle involved at the end of the simulation. The first thing to note is that there are two peaks formed near 0 and  $\pi$ , these two angles represent the two opposite beam directions.

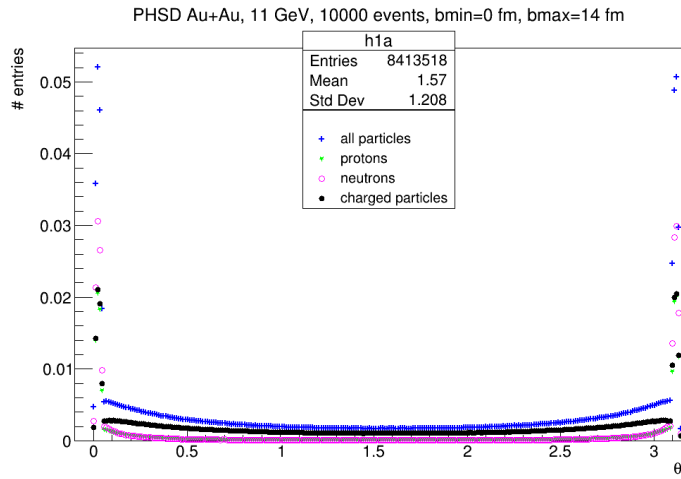


Figure 14: Distribution of the angle  $\theta$  (vertical axis in logarithmic scale) coming from different ensembles of the particles

These two peaks came from the spectator nucleons (non-colliding nucleons that keep

moving in the beam-direction), as expected most of these are neutrons, since these conform most of the mass of the nucleus. Following these are the protons, which conform virtually all of the charged particles in the peak regions. I had to use the logarithmic scaling in the vertical axis since the multiplicity was prominent around the peaks, this was because most of the collisions were non-central and most of the nucleons served as spectators.

The velocity in the beam direction of the produced particles can be analyzed in the pseudorapidity distribution, which also is in function of the angle  $\theta$ . The first and most clear relation between the  $\theta$  and  $\eta$  distributions is the presence of two peaks of high multiplicities at certain distance from the center of the horizontal axis, as seen in Figures 15 and 14.

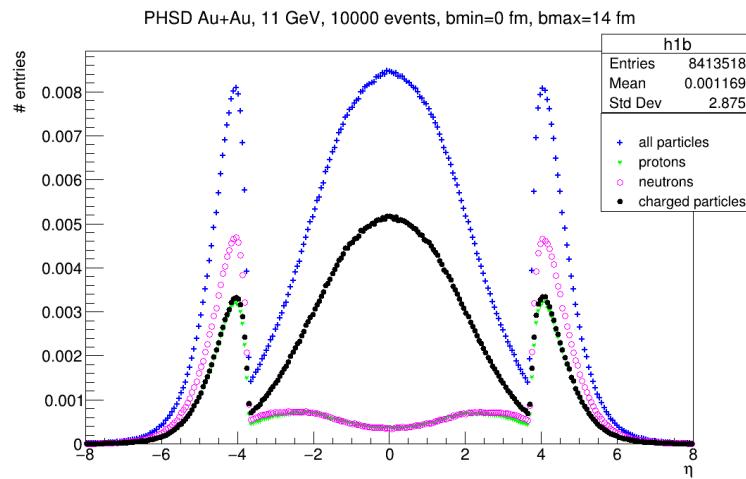


Figure 15: Distribution of the pseudorapidity  $\eta$  coming from different ensembles of particles

Looking at the geometric representation of the pseudorapidity, present in Fig. 8 it's easy to note that these two peaks came from the non-central events where a fraction of nucleons keep traveling in the beam direction as the in  $\theta$  distribution, present in Figures 15 and 14. The principal difference between these two distributions is that in the pseudorapidity one, the high multiplicities coming from hard interactions with high  $p_T$  (coming from the overlap region between the nuclei) are more evident, and actually, the overall amount of particles (blue lines) generated at  $\eta = -4$ ,  $\eta = 0$  and  $\eta = 4$  are comparable.

The same idea from the last two distributions is inherited to the ones for charged

pions. The principal difference from the others is the absence of high multiplicities at the beam directions, this is because none of the particles that form the nucleus are pions and therefore the spectators that follow the beam directions are just formed by neutrons and protons.

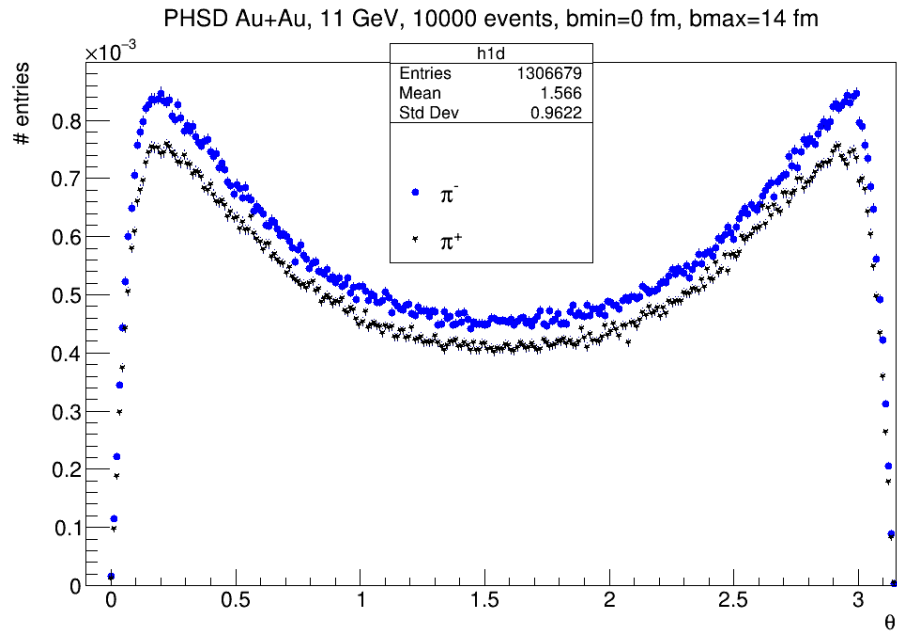


Figure 16:  $\theta$  distribution for charged pions

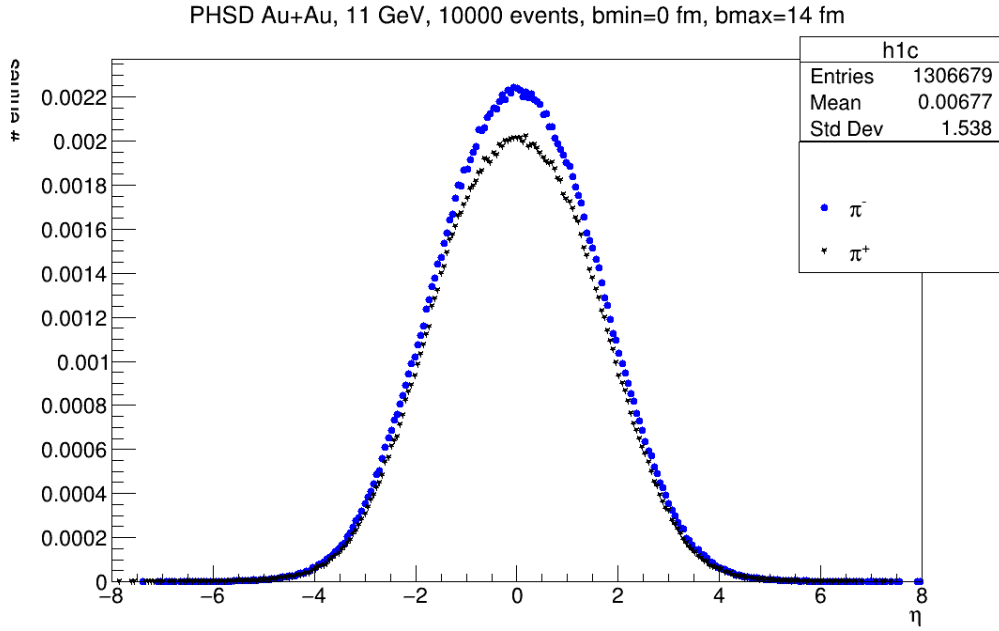


Figure 17:  $\eta$  distribution for charged pions

Another interesting thing to note here is that there is a slightly difference in the production of pions (black lines) and anti-pions (blue lines), seen in both Figures 16 and 17, this disequilibrium of anti-matter over matter production could be explained by the difference of 117 neutrons and 79 protons in the Au nuclei and the following reactions in the overlap regions

$$\begin{cases} p^+ \rightarrow n^0 + \pi^+ \\ n^0 \rightarrow p^+ + \pi^- \end{cases} \quad (10)$$

#### 4.1.4 UrQMD, 10 000 events, 11 GeV, Min.Bias

For the UrQMD generator there's no option for parallel events for a given selection of impact parameters, therefore in this case all 10 000 events are generated with fixed value for  $b$  following the Min.Bias distribution.

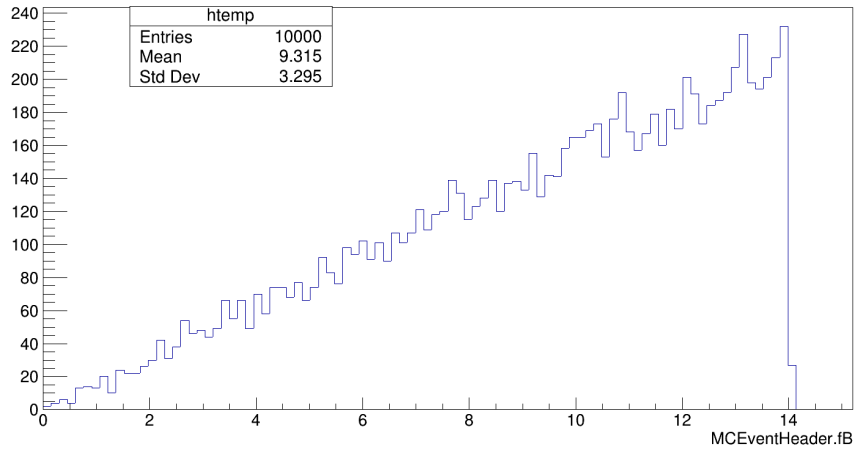


Figure 18: Non normalized impact parameter distribution for 10 000 UrQMD events

Since we have more statistics for this simulation, the linear relation of the impact parameter selection and the Min.Bias probability distribution is graphically more noticeable than the other cases.

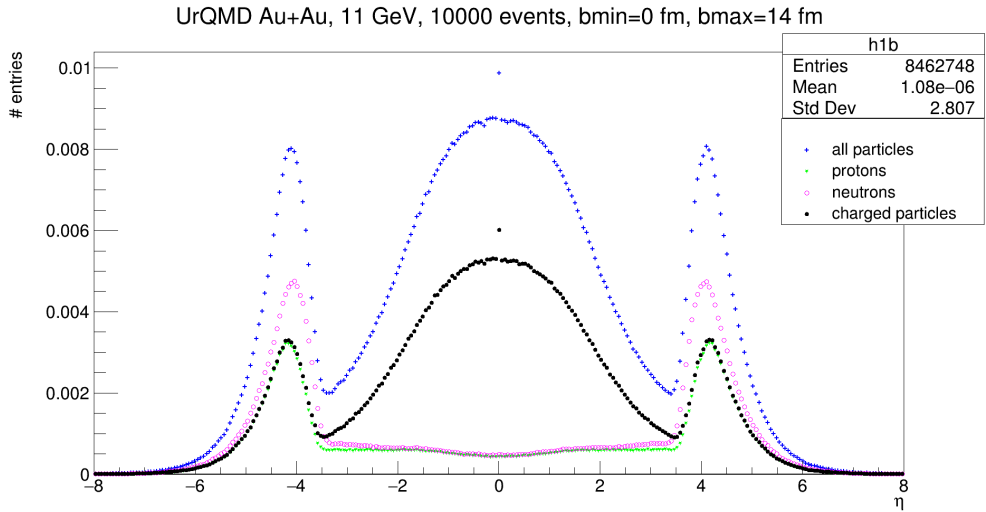


Figure 19: Pseudorapidity distributions for 10 000 UrQMD events

The graphic relation  $\theta$  and  $\eta$  relation was established in the previous simulations, so directly jumping to the pseudorapidity distributions it is virtually impossible to identify graphically if there is the difference (besides the overall multiplicity that could be explained by the pseudo-randomness of the events) between the physics processes involved in either generator.

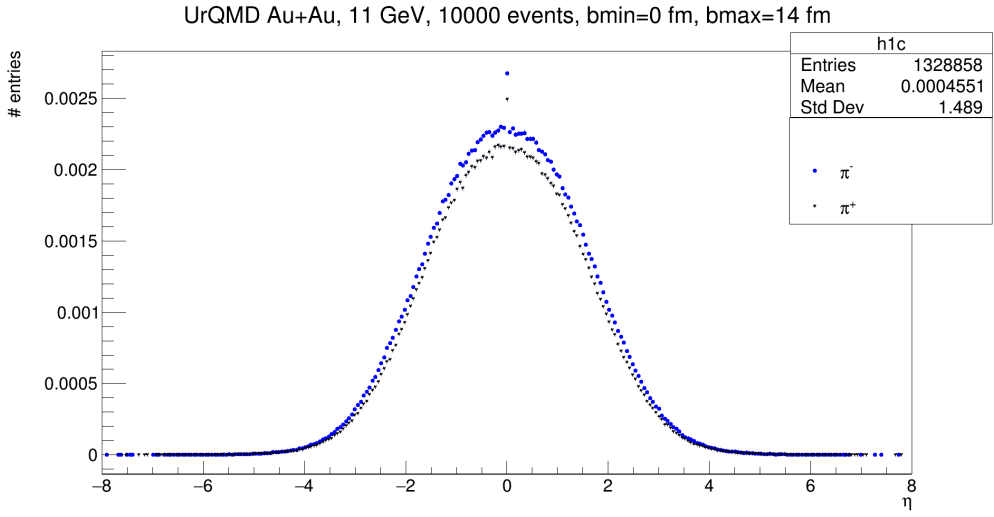


Figure 20: Pseudorapidity distributions for charged pions

Nevertheless, looking at the pseudorapidity distribution for charged pions and the gap between  $\pi^-$  and  $\pi^-+$  it's clear that that there is a level of affinity at nuclear interaction level between both generators.

To search for evidence that could enlight the difference of the physics processes at theoretical level for the models implemented in the PHSD and UrQMD generators it is imperative to implement the interactions at detector levels. To do it so, in the following chapters I will work with the MPDROOT framework which allows the use of specific libraries alongside with ROOT and Geant4 (for GEometry AND Tracking) to transport the generated particles, simulate and work with the geometries of some of the detectors planned to use in the MPD experiment. This text will focus on the pseudorapidity regions covered by the BE-BE and MBB detectors (see Fig. 21)

## 4.2 Results using mpdroot framework

The next pseudorapidity distribution histogram was made by Luis Valenzuela from the *Universidad de Sonora* and it shows the regions where various detectors from the MPD experiment attempt to cover. In this text I will focus on the regions covered by the BE-BE and MBB detectors.

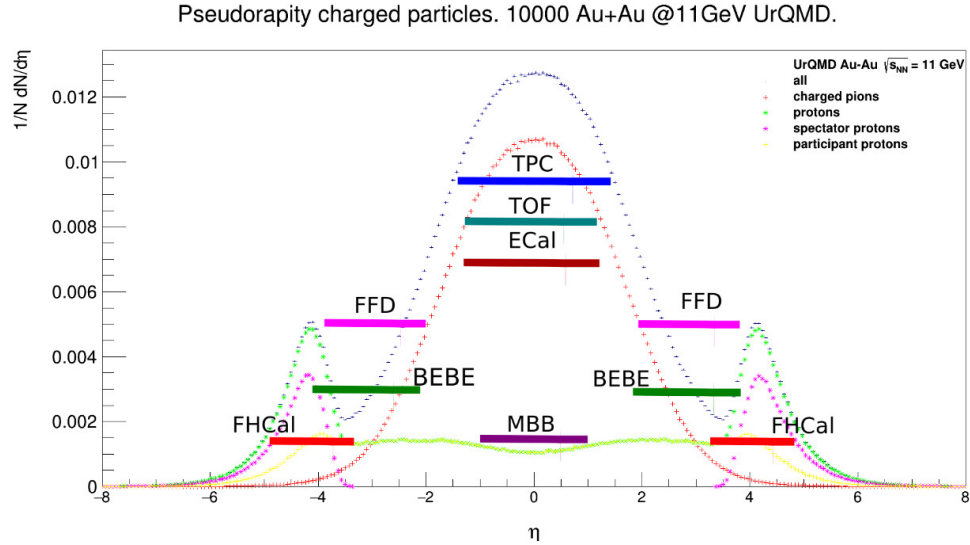


Figure 21: Coverage regions of different detectors from the MPD experiment. The code for this distribution was written by Luis Valenzuela

### 4.2.1 BE-BE detector

The concept of the BE-BE detector consist of two hodoscope detectors located 2 meters away form the interaction point on each side. The geometry consists of an array of 162 hexagonal cells made of plastic scintillator arranged in six concentric rings which cover the pseudorapidity values inside the range of  $1.9 < |\eta| < 3.97$ , the data gathered by the BE-BE can be used for the reconstruction of some observables of interest such as the multiplicity of charged particles, centrality determination and the event plane resolution, as well to discriminate actual events coming from interacting nuclei and beam-gas events coming from residual gas atoms inside the pipes. [13]

For the analysis of the particles detected, there are two principal points to see in the resultant plots. As I show in the latter plot in fig. 21) the BE-BE attempts to cover certain regions of pseudorapidity, at generator level, all distributions are taken as if we were using an "ideal detector" which gives us all the information coming form the

simulated events. In real life, the existence of such detector is impractical if the aim is to probe certain physical phenomena as many of the information given by this detector can be considered noise for that purpose. With this in mind, there are regions of particular interest for certain detectors, and the regions that the BE-BE detector covers in the latter pseudorapidity distribution corresponds to two lid-like detectors in each side of the beams. The following histograms shows the pseudorapidity distributions just for the regions of the BE-BE.

It's important to note here that the only effect of the BE-BE detector in the next plot is just that of selecting the coverage regions for the pseudorapidity, in other words, all of the information given at generator level (with slight differences coming from the fact that the MPDROOT is in constant development and updating) is given here just in the BE-BE region.

The series of histograms in the following subsections were drawn taking different macros as a basis, these were written by Luis Valenzuela and Pedro Nieto from the *Universidad Autónoma de Sinaloa*

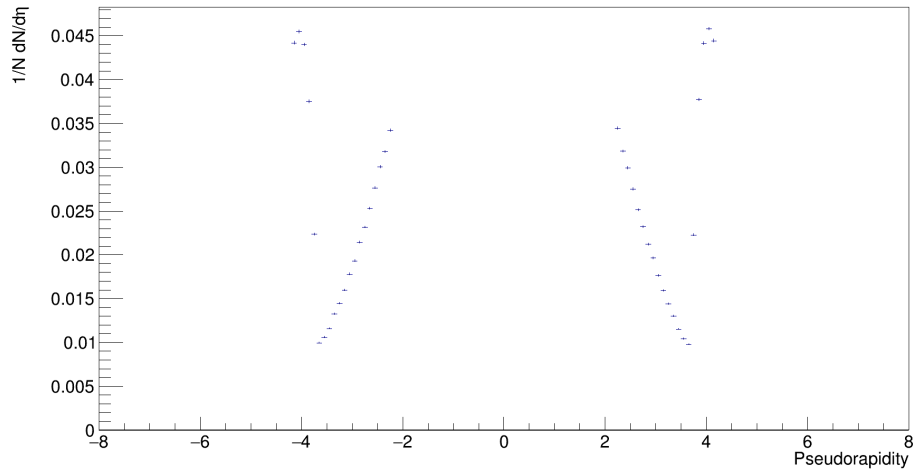


Figure 22: pseudorapidity distribution corresponding to all the particles given by the PHSD is the BE-BE region

Taking a look at the pseudorapidity distribution in figure 23, the number of entries is significantly reduced, this is a direct consequence of the implementation of the BE-BE detector as just a fraction of the generated particles will actually have the energy necessary to get through the cells and count as an actual hit.

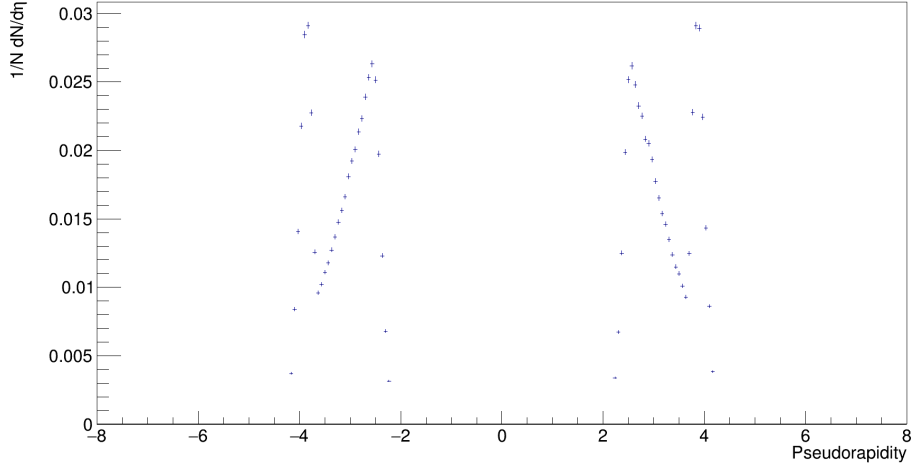


Figure 23: Pseudorapidity distribution for all the particles that hit the BE-BE detector

The following diagrams show the geometrical display of the BE-BE detector and the hit distributions for each of the six rings that conform it.

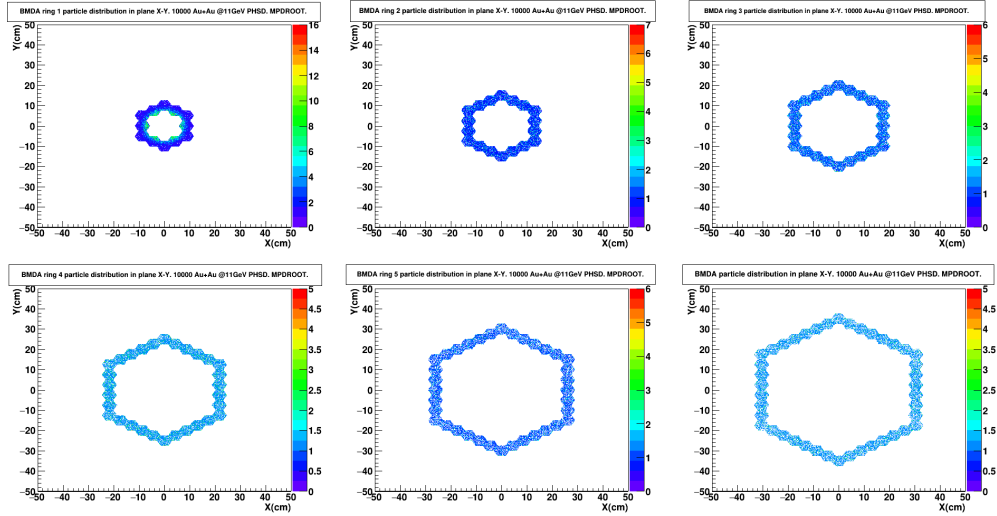


Figure 24: Individual hit distributions of one side of the BE-BE detector for every ring

These rings cover a fixed ranges of pseudorapidities inside the overall range of the BE-BE, where the first ring is the closest to the beam directions. With that said, if we take a look at the pseudorapidity distributions in the previous chapter (see Figs. 15,

17) we can expect a high density of hits in the first ring and a gradual decrease in hits density the more external the rings are, which in precisely what is present in figures 25 and 24

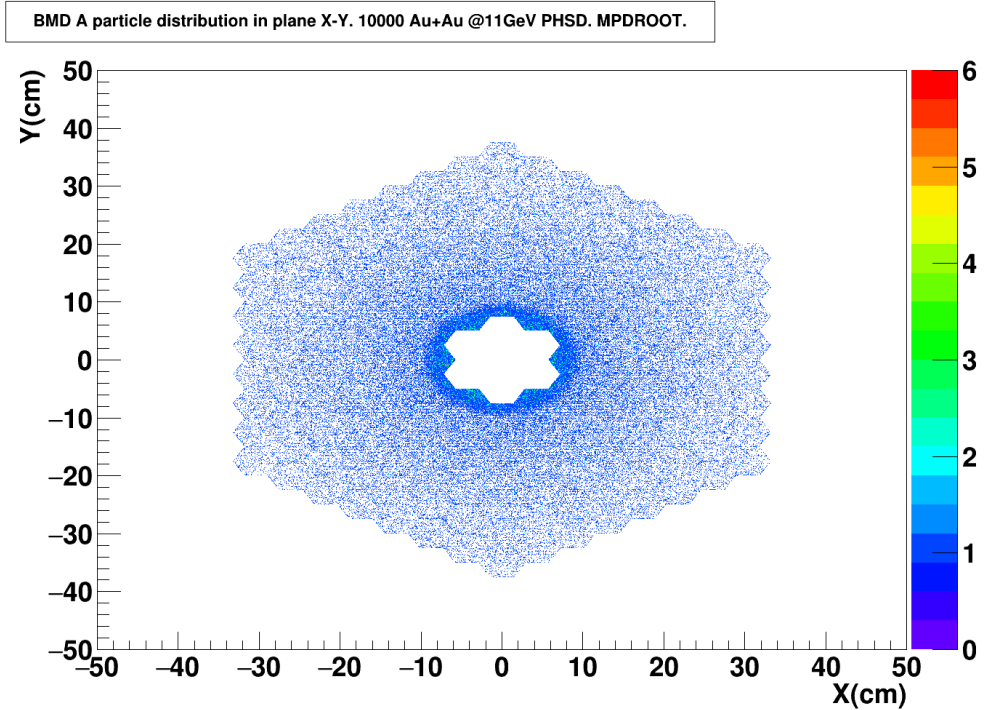


Figure 25: Hit distribution for all rings

The previous information can also be represented in a multiplicity distribution per cell and as expected, the first twelve cells coming from the first ring are the ones with the greatest multiplicity.

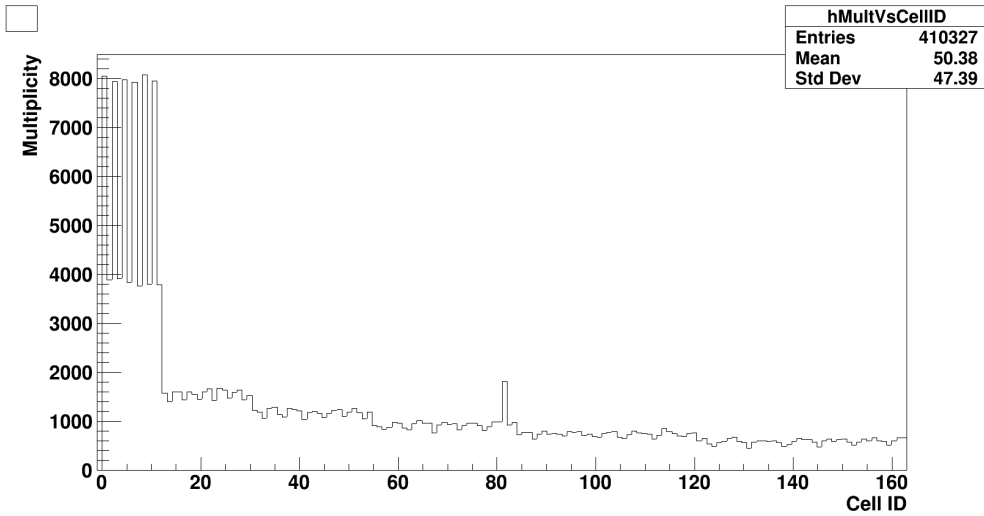


Figure 26: Multiplicity distributions per cell

#### 4.2.2 Inner detector MBB

The MBB detector is intended to be placed around the interaction point, therefore it will be possible to probe particles with higher values of transverse momentum in very central values of the pseudorapidities, ranging from  $\eta = \pm 1.01$ .

The proposed geometry consists of 16 strips of 60 cm around the interaction point in a cylinder-like arrangement. Each strip is made of 20 plastic scintillator cells, each one coupled to 4 Silicon Photo Multipliers, with a total of 320 squared cells and 1,280 Silicon Photo Multipliers

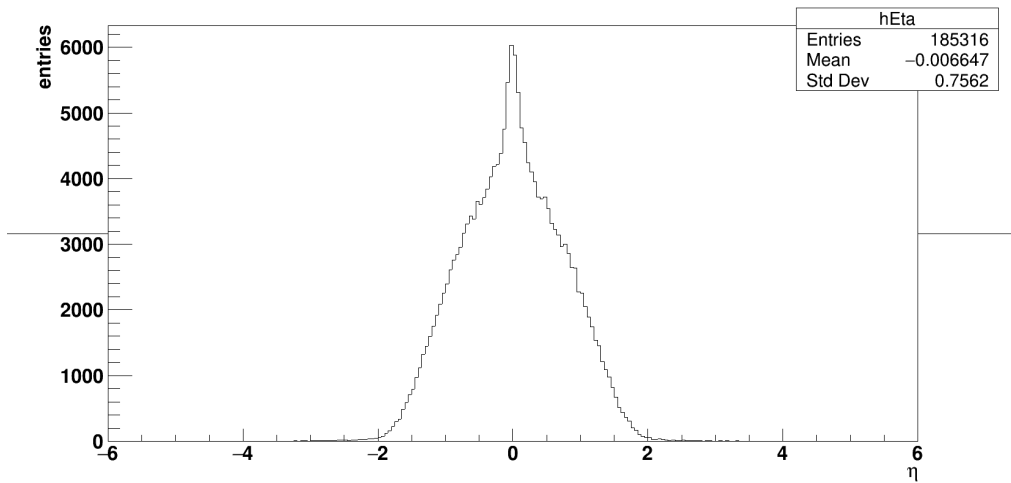


Figure 27: The pseudorapidity region intended to probe by the MBB detector

The following diagrams show the geometry display of the MBB and the distribution of hits around the whole detector, taking different planes as the display reference, these results and the multiplicity distribution (Fig. 31) were made taking the macro written by Luis Valenzuela.

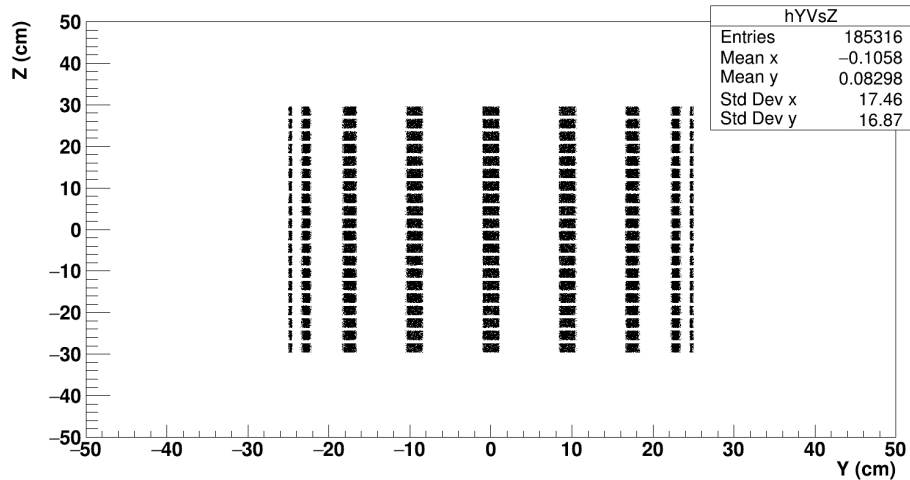


Figure 28: Distribution of hits in the y-z plane

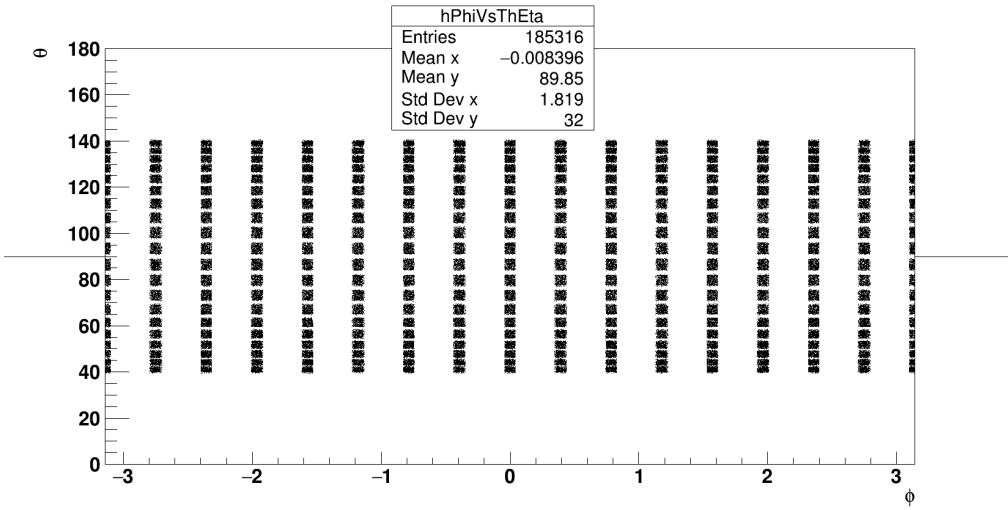


Figure 29: Distribution of hits spanned by the angles  $\phi$  that covers the azimuth of the cylinder and  $\theta$  that goes covers both beam directions

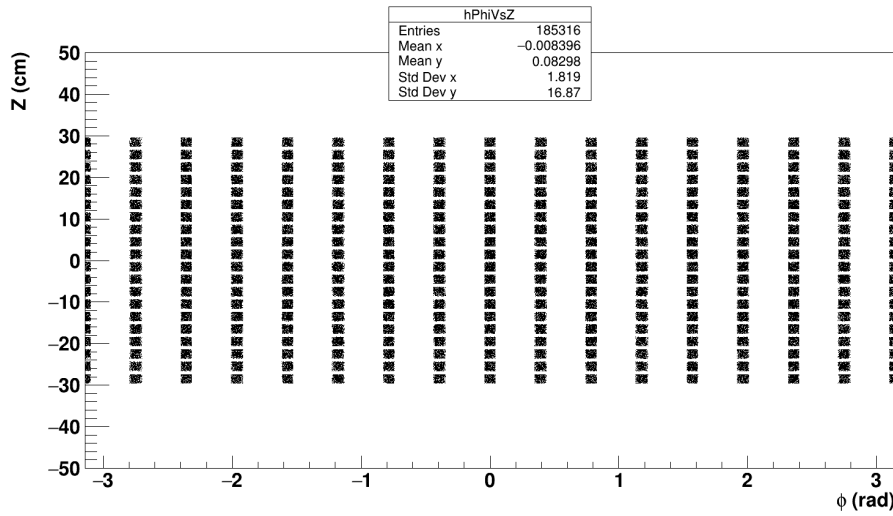


Figure 30: Distribution of hits spanned by the the angle  $\phi$  and the z-axis

In the next plots, the multiplicity distribution per cell of charged particles is displayed. The particle multiplicity of both generators show the same order, with slight differences that could came for the relatively low statistic. An amount of of 16 peaks can be seen in Figs. 31 and 32, which correspond to the 16 strips around the interaction point. There is a bin in the histograms that shows a particular high multiplicity overall

the others, this phenomena is shared in both generators and it could be an evidence of particles with extremely high valued transverse momentum coming from head-on collisions between nucleons which reactions happen to be with a high amount of produced particles.

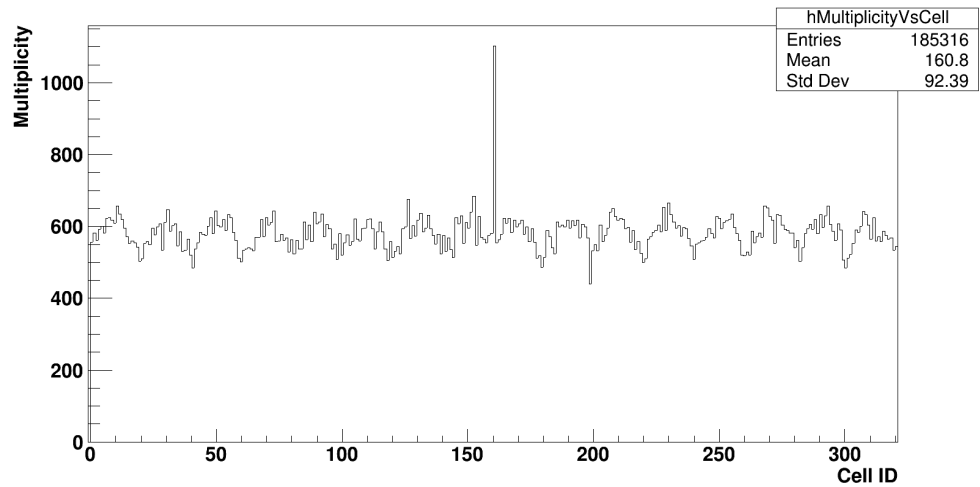


Figure 31: Multiplicity distribution per cell with the PHSD generator

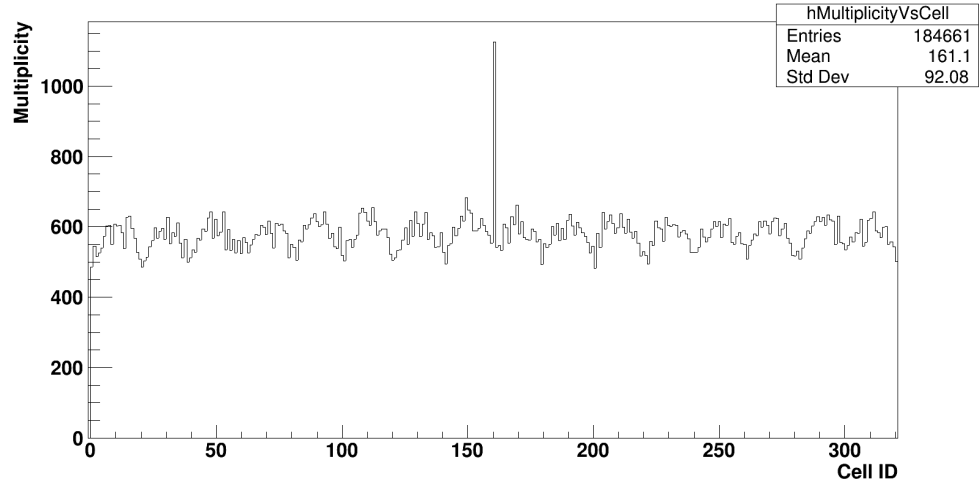


Figure 32: Multiplicity distribution per cell with the UrQMD generator

The following plots are the ones that show more differences between both generators.

For the average number of hits in the UrQMD generator appears to be approximately three orders of magnitude above the PHSD for the first as it is seen in Figs. 33 and 34, second and third rings getting more comparable starting from the fourth ring, reaching a peak more or less over the same value and maintaining nearly the same proportion for the rest of the rings. The scale in the y-axis appears to be automatically displayed, and the PHSD distribution shows a higher resolution given the intermediate values on the vertical lacking in the UrQMD distribution. Even though the PHSD simulation was performed with 1000 impact parameter values with Min.Bias distribution each one with 10 parallel events, it appears the statistical error was significantly reduced, giving a more homogeneous hit distribution.

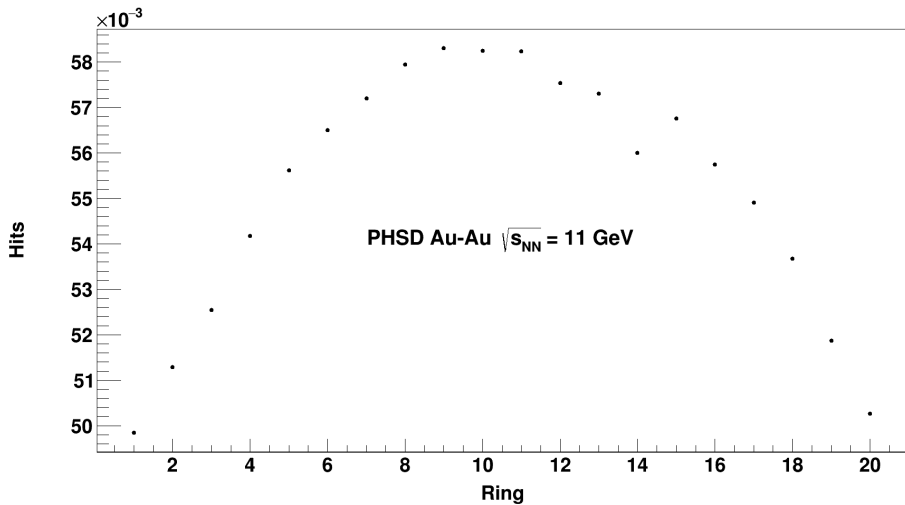


Figure 33: Number of average hits per ring with the PHSD generator

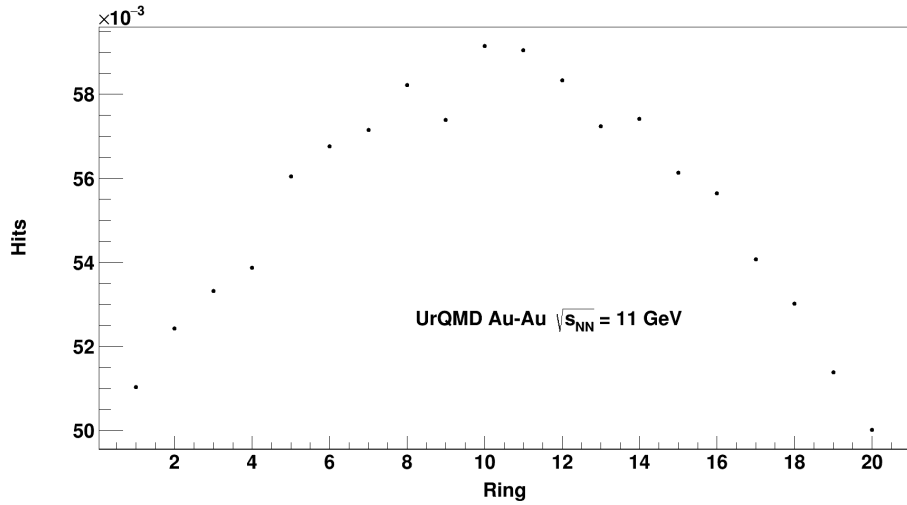


Figure 34: Number of average hits per ring using UrQMD generator

An analog behaviour can be seen in the the deposited energy distributions for both generators, as it can be appreciated in Figs. 35 and 36. Here the change in concavity is given that the hits are defined by the amount of particles that totally cross a given cell, therefore if the kinetic energy of a particle is high enough, as for the ones with high transverse momentum, it will have less time to transfer the energy into the detector.

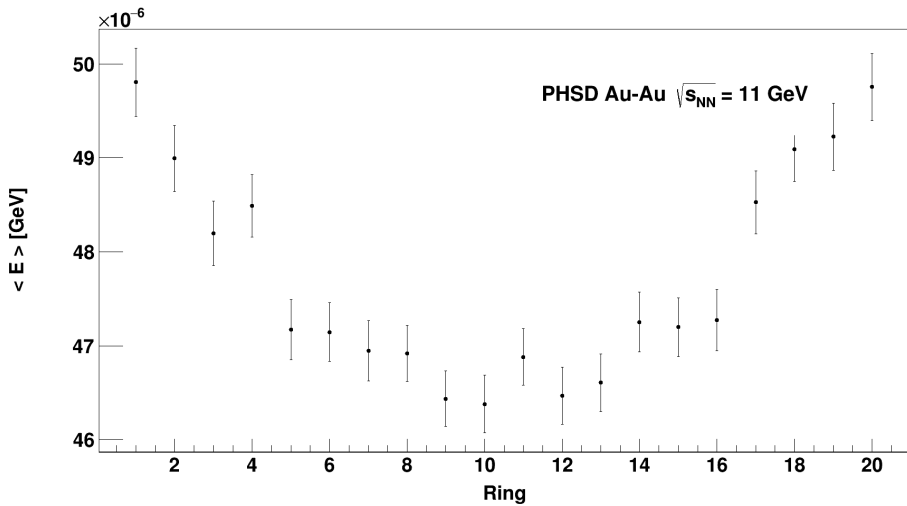


Figure 35: Deposited energy per ring using PHSD

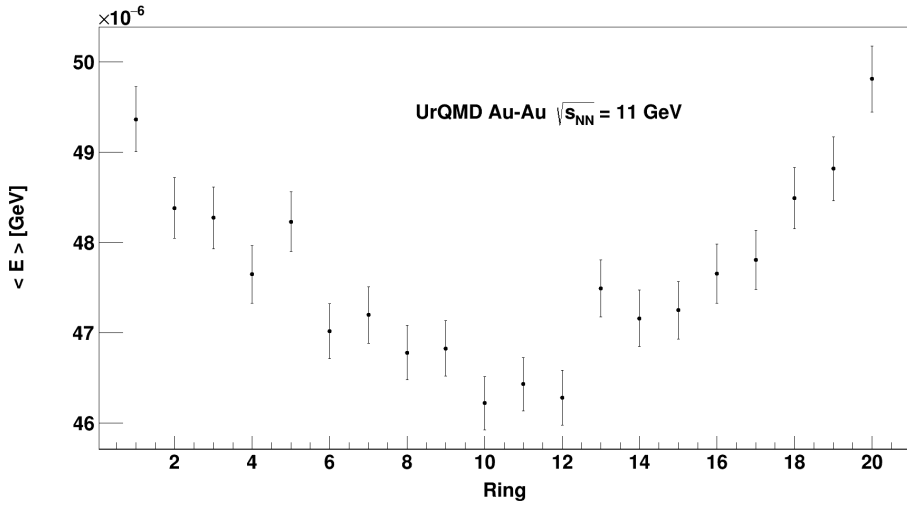


Figure 36: Average energy deposited per ring using UrQMD

These observations might be a reflect of different physics phenomena inherent on the generators, which are noticeable in regions of low multiplicities given the reduction of background noise data. Furthermore, these observations may be important for the miniBeBe prototype since the energy deposited per cell shows in some way the amount of radiation that the detector is absorbing.

## 5 Conclusions and future work

During the documentation of this text, my results were constantly discussed during regular meetings of the MexNICA off-line/Analysis group. The plots in the section of results at generator level were actually validated during the celebration of the first computational workshop, where I presented my results to the rest of the students and other members of MexNICA. This workshop, given on February 2020, was essential for the advance of this investigation, since was during the week that the workshop was held when some of the students, me included, learned the basics of the MPDROOT framework used to transport particles and simulate their effects on the detectors.

The difference in the results obtained for the MBB detector using PHSD and UrQMD have an important impact on the article for the conceptual design for the miniBeBe (CDR) that currently the MexNICA group is working on. The last four distributions for the energy deposited and the average number of hits per ring using both generators are the ones that show a significant difference in between, this has two important implications in the further work for the CDR documentation: The first comes from the fact that the distribution for energy deposited show a different threshold for the radiation that the MBB is holding up, this is because both simulations were performed using the maximum value in energy range planned to use NICA ( $\sqrt{s_{NN}}=11$  GeV); the second one is that these differences may be a direct evidence of the physics involved in the different models in which each generator relies on. The later point is reinforced taking into account that some of the interactions involved in the PHSD can be turned off, and there is a full history from which interactions the generated particles come from. Also, to disentangle these questions, the implementation of PHSD simulations with more events and different nuclei species may be used to reduce the statistical error and search for different outcomes with the same physics fundamentals.

## References

- [1] W. Cassing and E.L Bratkovskaya, *Parton-hadron dynamics: An off-shell transport approach for relativistic energies*, Phys. Rev. C 78 (2008) 034919, arXiv:0808.0022 [hep-ph]; *Parton-Hadron-String Dynamics: an off-shell transport approach for relativistic energies*, Nucl. Phys. A 831 (2009) 215-242, arXiv:0907.5331 [nucl-th].  
<https://theory.gsi.de/~ebratkov/phsd-project/PHSD/index2.html>
- [2] <http://mpd.jinr.ru/purposes-of-the-mpdroot-framework/>

- [3] V. Firese, *Heavy-ion physics at high baryon densities*, EPJ Web Conf. 95 (2015) 03010.
- [4] Maria Elena Tejeda-Yeomans, *Heavy-ion physics: freedom to do hot, dense, exciting QCD*, Contribution to: CLASHEP2019, e-Print: 2004.13812 [nucl-th].
- [5] A. Kovalenko, et. al. (NICA Collaboration) *Status and Perspectives of the NICA Project* PoS SPIN2018 (2019) 007. V. Kekelidze, et. al. *Feasibility study of heavy-ion collision physics at NICA JINR*, Nucl.Phys.A 967 (2017) 884-887.  
<http://nica.jinr.ru/physics.php>
- [6] S. A. Bass, et. al, *Microscopic Models for Ultrarelativistic Heavy Ion Collisions* Prog. Part. Nucl. Phys. 41 (1998) 225-370; M. Bleicher, et. al., *Relativistic Hadron-Hadron Collisions in the Ultra-Relativistic Quantum Molecular Dynamics Model* J. Phys. G: Nucl. Part. Phys. 25 (1999) 1859-1896.  
<https://urqmd.org/>
- [7] Kh. U. Abraamyan, et. al. *The MPD detector at the NICA heavy-ion collider at JINR*, Nucl.Instrum.Meth.A 628 (2011) 99-102.
- [8] W. Busza, K. Rajagopal and W. van der Schee, *Heavy Ion Collisions: The Big Picture and the Big Questions*, Ann.Rev.Nucl.Part.Sci. 68 (2018) 339-376 e-Print: 1802.04801 [hep-ph].
- [9] <http://mpd.jinr.ru/experiment/>
- [10] R. Sahoo *Relativistic Kinematics*, e-Print: 1604.02651 [nucl-ex].
- [11] K. Reygers, *Quark-Gluon Physics*, (2017)  
[https://www.physi.uni-heidelberg.de/~reygers/lectures/2017/qgp/qgp\\_ss17\\_01\\_intro.pdf](https://www.physi.uni-heidelberg.de/~reygers/lectures/2017/qgp/qgp_ss17_01_intro.pdf)
- [12] <https://github.com/dchezz/Thesis>
- [13] M. Alvarado, et. al., *A beam-beam monitoring detector for the MPD experiment at NICA*, Nucl.Instrum.Meth.A 953 (2020) 163150.